博士論文

A Study on a New Caging Method Aimed at Visible Light-Activable Anticancer Drugs

（可視光活性化抗がん剤を目指した新しいケージド手法の研究）

北海道大学大学院　生命科学院

生命融合コース

分子情報科学研究室

斉　嘉俊　（QI JIAJUN）

2024/09

Table of Contents

1. Introduction

Small-molecule inhibitors have recently emerged as promising therapeutic agents for cancer treatment.[1, 2] However, their effectiveness is often hindered by critical issues such as side effects resulting from the inability to confine drug activity to a limited region and the development of resistance.[3] Therefore, alongside the quest for new, efficient, and targeted anti-tumor agents, exploring innovative approaches to enhance their selectivity and localized action is essential.

Various internal and external triggers have been previously employed to regulate drug activity.[4-7] Several light-mediated approaches, including optogenetics,[8] photodynamic therapy (PDT),[9] and photopharmacology,[10] have been developed in recent years. However, the therapeutic application of optogenetics is limited by the need for genetic alterations, and clinically adopted PDT lacks specificity for precise molecular targets, making it primarily suitable for the destruction of tumors or infected tissues.[10a]

Fortunately, the field of photopharmacology has emerged to provide a potential solution to these challenges. Photopharmacological agents are crafted by incorporating a photoresponsive component, such as a photocaging group[11] or photoswitch,[12] into a drug molecule, enabling dynamic control over its activity. Notable examples include the modification of well-established anticancer drugs like imatinib[13] and vemurafenib[14] with light-sensitive groups such as 4,5-dimethoxy-2-nitrobenzyl and *o*-nitrobenzylic photoprotective groups, effectively transforming them into caged drugs (prodrugs) that are inactive until exposed to UV (365 nm) light.

I aimed to develop a general caging method targeting the triarylimidazole moiety, which is a crucial structural component in various small-molecule inhibitors used to target different kinases in anticancer treatment.[15, 16] Among them, **SB431542**[17, 18] is a triarylimidazole-based small-molecule inhibitor (Scheme 1) that has garnered significant attention due to its specificity and potency as an inhibitor of TGF-β type 1 receptors (TGF-β R1), specifically ALK4, ALK5, and ALK7. **SB431542** effectively targets the tumor-promoting actions of TGF-β in human cancer cells, including cell migration, invasion, and secretion of vascular endothelial growth factor. Additionally, **SB431542** remarkably inhibits colony formation by late-stage colon cancer cells (HT29).

Balancing the anti-proliferative property of TGF-β[19, 20] in normal cells while sufficiently blocking its tumor-promoting effect in cancer cells is crucial.[21] To achieve this, I developed photocaged forms of **SB431542** (**1** and **2**) by introducing -$N(CH_3)_2$ (dimethylamino) and -$N(CH_3)CH_2COOH$ (N-methyl-(N-hydroxycarbonylmethyl) amino) groups, respectively, on the carbon atom of the imidazole ring (Scheme 1), which intrinsically modulated the core structure from planar imidazole to tetrahedral 2*H*-imidazole. The formed C–N bond was cleaved upon visible light irradiation, reforming the original bioactive **SB431542**. Despite lacking bulky aromatic moieties in their photoremovable groups, caged **1** and **2** exhibited visible light sensitivity due to absorption by the triaryl-2*H*-imidazole structure. This sets them apart from typical UV-responsive *o*-nitrobenzyl, visible light-responsive coumarin, cyanine, and BODIPY-based photocaging groups.[22]

Using photocaged **SB431542**, I demonstrated selective inhibition of cell migration upon visible light irradiation via wound healing assays conducted with human breast cancer cells. This caging method targeting imidazole-based drug molecules presents a widely applicable strategy to regulate drug activity, thereby minimizing adverse effects and reducing the risk of developing drug resistance in cancer treatment.

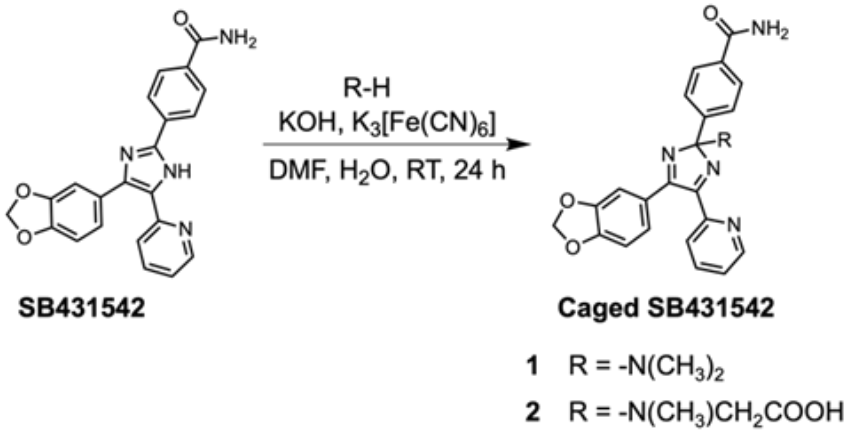

Scheme 1. Synthetic route to obtain caged forms of **SB431542** (**1** and **2**) and structures of newly designed caged

2. Results

2.1 Molecular Design and Synthesis

I successfully synthesized **1** from **SB431542** via ferrocyanide oxidation in the presence of dimethylamine in *N*, *N*-dimethylformamide (DMF). As an alternative, I synthesized **2** from **SB431542** by introducing the N-methyl-(N-hydroxycarbonylmethyl) amino group to enhance the molecule's water solubility (Scheme 1). The detailed synthetic procedures to obtain **1** and **2** are presented in the Supporting Information (Schemes 2 and 3, respectively). The synthesized compounds were characterized using ^{1}H NMR, ^{13}C NMR, and mass spectroscopy (Figures 1–6). Compound **2** was soluble in water up to a concentration of at least 700 μM, which was significantly higher than the maximum solubility of Compound **1**. (Figure 7).

I investigated the photoresponsive properties of **1** and **2**. To characterize the photoreactivity of **1**, I measured its absorption spectrum in a 1:1 acetonitrile and water mixture at 25 °C (Figure 8), which revealed two distinct absorption maxima at 262 and 359 nm. After irradiating the solution at 405 nm, these peaks disappeared and a single absorption maximum at 326 nm emerged, coinciding with the absorption maximum of SB431542. Notably, irradiation at 405, 430, and 450 nm could induce photoreaction of 1, leading to the formation of SB431542 (Scheme 4 and Figures 9, 10). Similar UV-visible absorption study indicated the formation of SB431542 from 2 upon 405 nm light irradiation (Figure 11).

1H NMR analysis was performed to further confirm the formation of SB431542 from 1 upon 405 nm light irradiation (Figure 12). The peaks in the 1H NMR spectrum of irradiated 1 matched those observed in the 1H NMR spectrum of SB431542, providing compelling evidence for the formation of SB431542 as a result of photochemical reaction. Similarly, 1H NMR analysis indicated the formation of SB431542 from 2 upon 405 nm irradiation (Figure 13).

High-performance liquid chromatography (HPLC) was employed to monitor the conversion of **1** to **SB431542** upon 405 nm light irradiation (Figure 14). The retention

times of **1** and **SB431542** were determined to be 10.8 and 6.6 min, respectively. I could confirm that the peak at 10.8 min was converted to the peak at 6.6 min upon 405 nm irradiation. Utilizing calibration curves derived from the correlation between the HPLC peak areas and their corresponding molar concentrations (Figures 15–16), I determined that the conversion efficiency of **1** to **SB431542** upon 405 nm irradiation was approximately 96%. The efficiency of converting **2** to **SB431542** under 405 nm light was 97%, as determined by changes in the UV-visible absorption spectra (Figure 11). The quantum yield of the photoreaction from **1** to **SB431542** at 405 nm estimated by the absorption spectra change was 0.44 and that for **2** was 0.34 (Figures 17-23 and Tables 1-2).

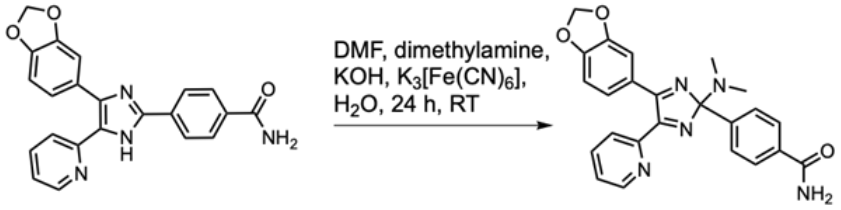

Scheme 2. Synthetic scheme for **1**.

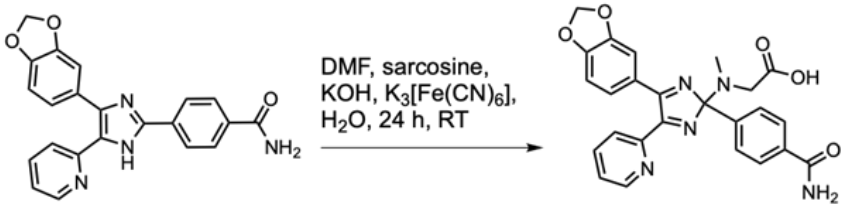

Scheme 3. Synthetic scheme for **2**

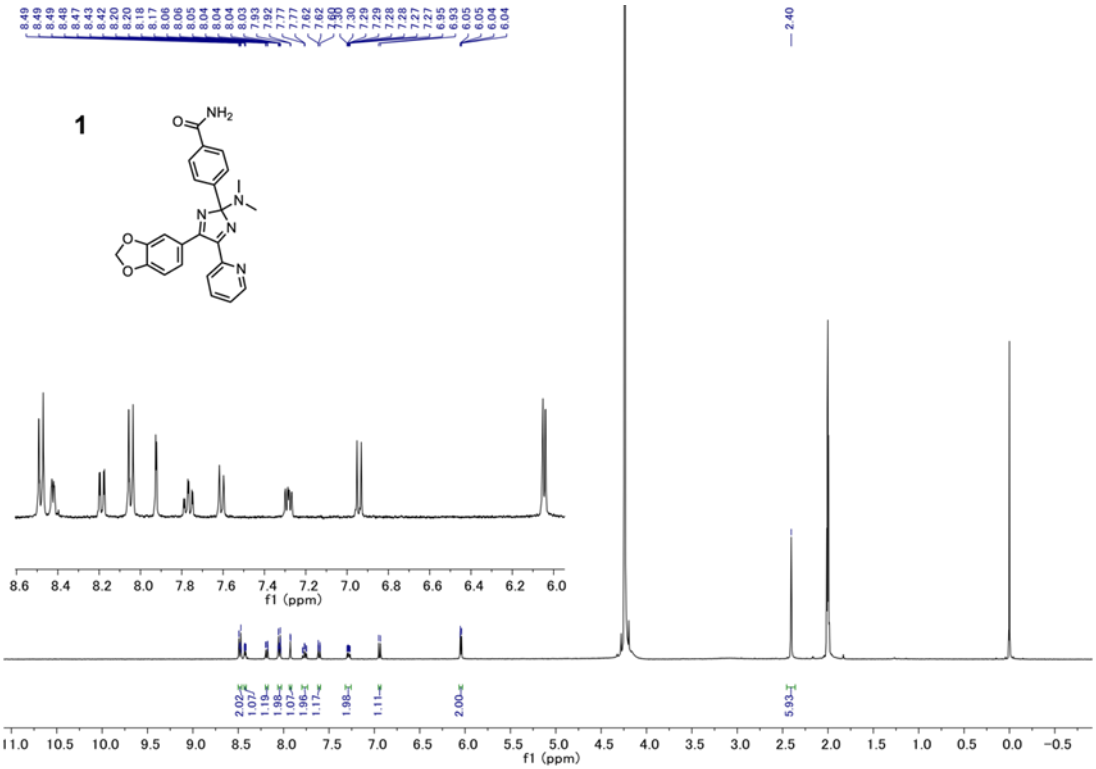

Fgure 1. ^{1}H NMR spectrum of **1** recorded in acetonitrile-d_3 and D_2O (1:1) mixture.

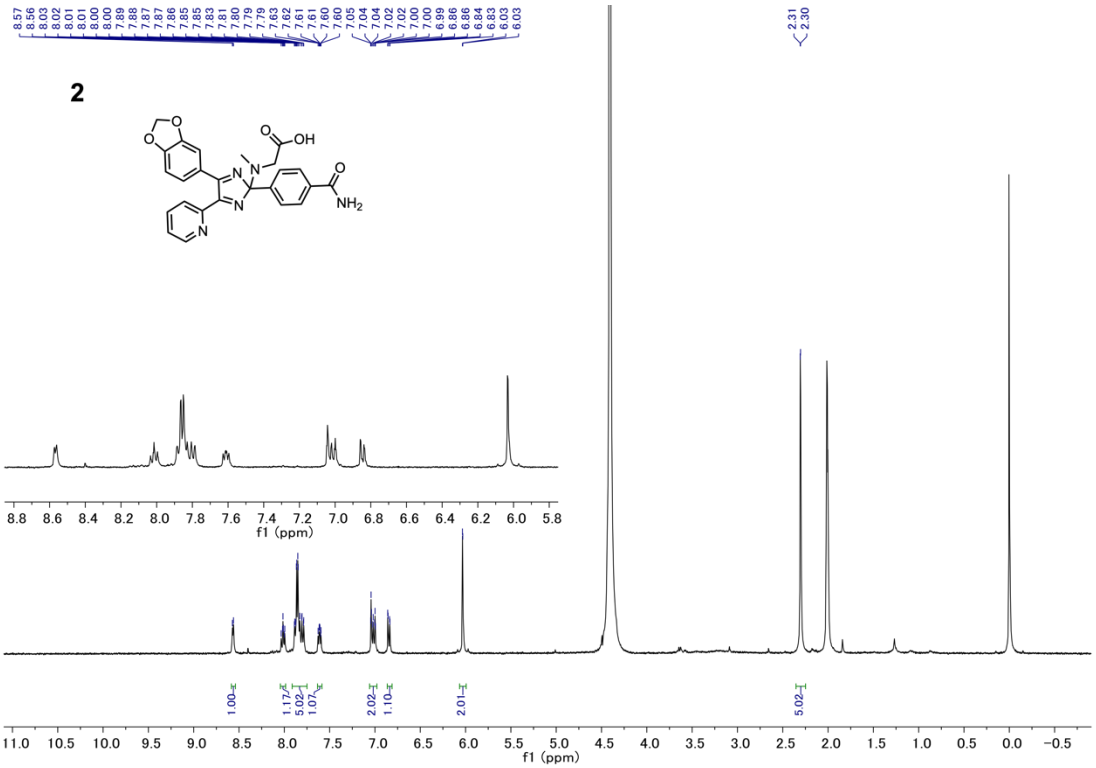

Figure 2. ^{1}H NMR spectrum of **2** recorded in acetonitrile-d_3 and D_2O (1:1) mixture.

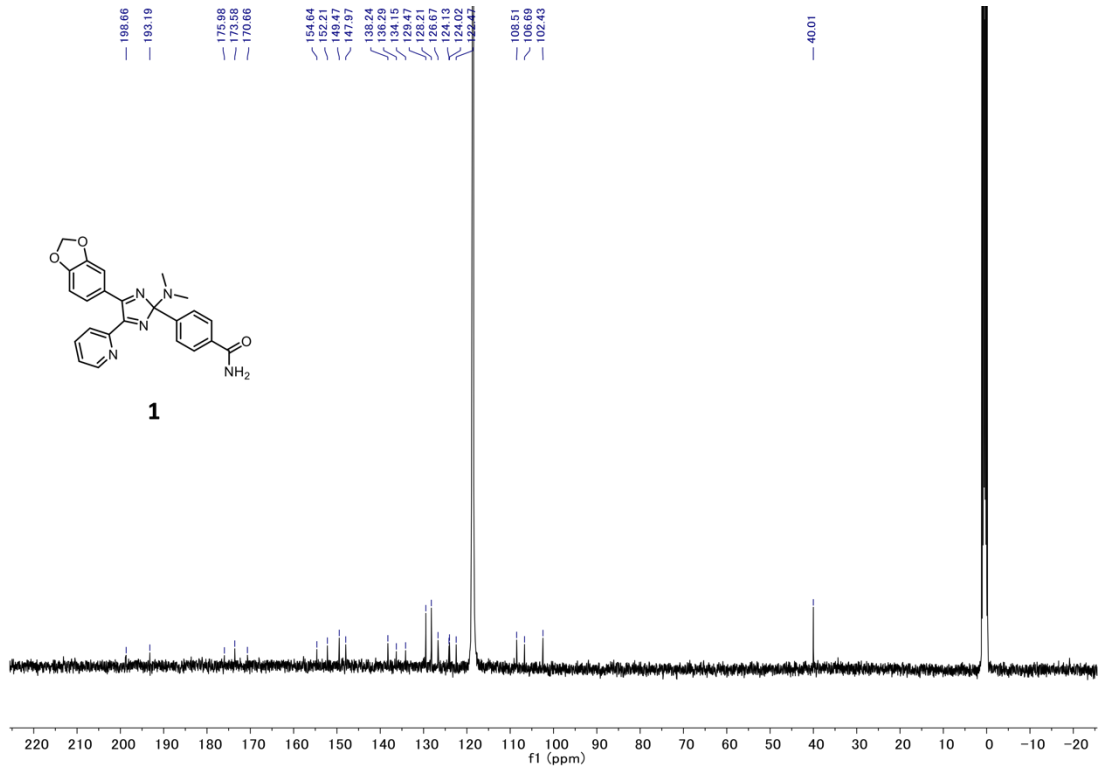

Figure 3. ^{13}C NMR spectrum of **1** recorded in acetonitrile-d_3 and D_2O (1:1) mixture.

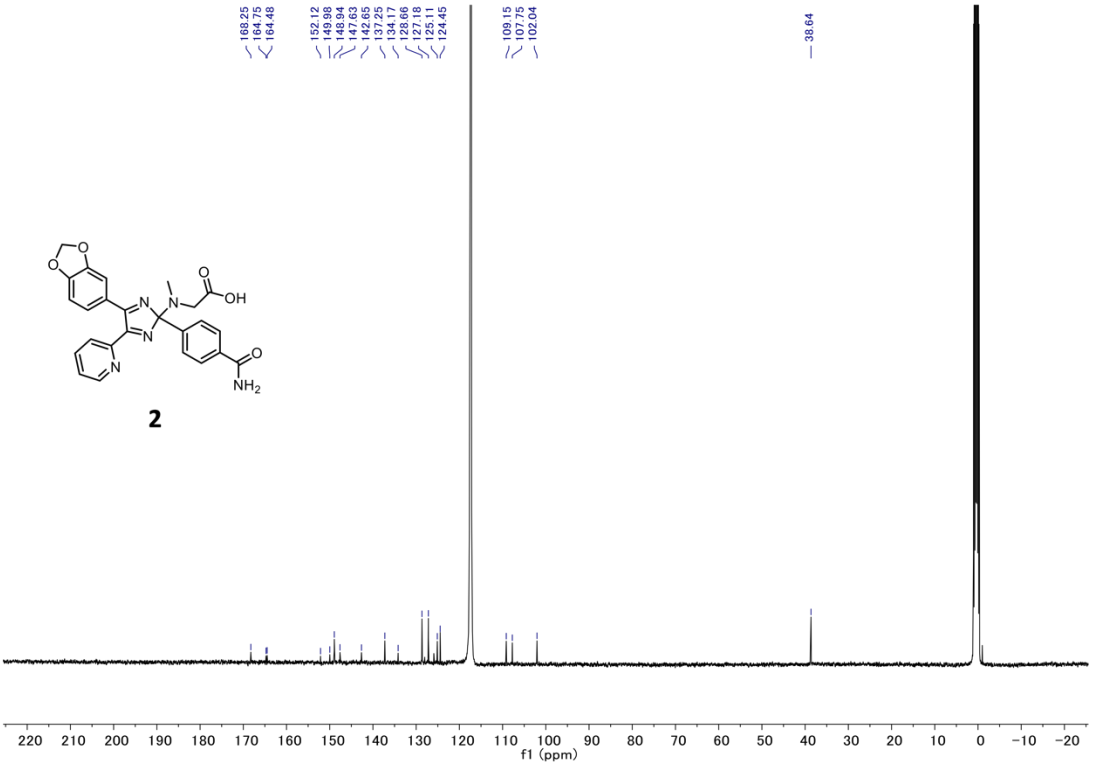

Figure 4. ^{13}C NMR spectrum of **2** recorded in acetonitrile-d_3 and D_2O (1:1) mixture.

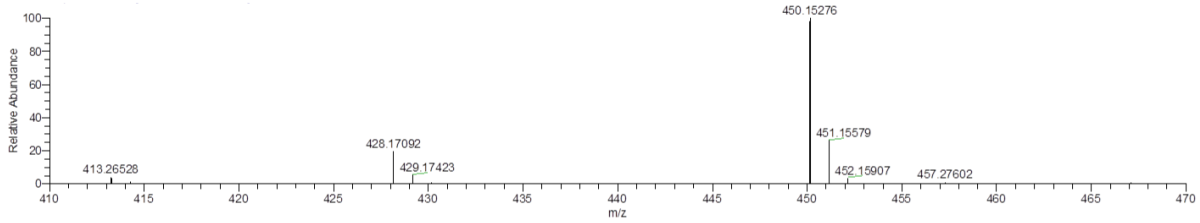

Figure 5. High resolution mass spectra (ESI) of **1** - m/z $[M+H]^+$ calculated for $C_{24}H_{21}N_5O_3$: 428.17226, found: 428.17092; m/z $[M+Na]^+$ calculated: 450.15421, found: 450.15276.

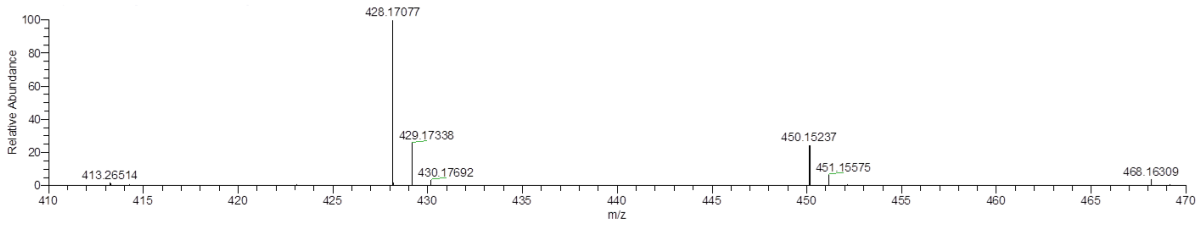

Figure 6. High resolution mass spectra (ESI) of **2** - m/z $[M+H]^+$ calculated for $C_{25}H_{21}N_5O_5$: 472.16209, found: 428.17077 indicating the elimination of a molecule of CO_2 $[M+H-CO_2]^+$; m/z $[M+Na]^+$ calculated: 494.14404 found: 450.15237 indicating the elimination of a molecule of CO_2 $[M+Na-CO_2]^+$.

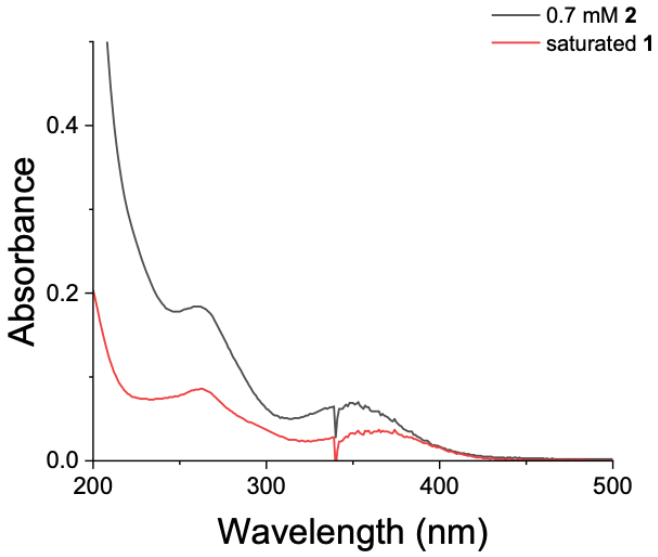

Figure 7. UV-visible absorption spectrum of **1** at saturated concentration (0.33 mM) and that of **2** at 0.7 mM concentration recorded in water (path length = 1 mm).

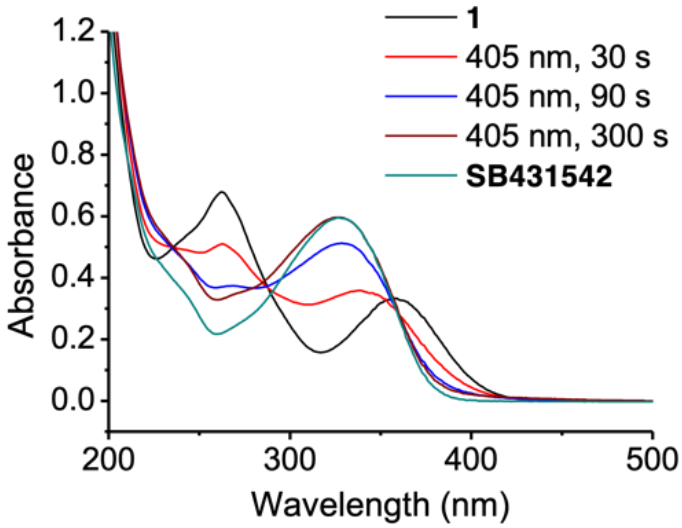

Figure 8. UV-visible absorption spectra of **1** upon irradiation with 405 nm light for different time periods and UV-visible absorption spectrum of **SB431542**.

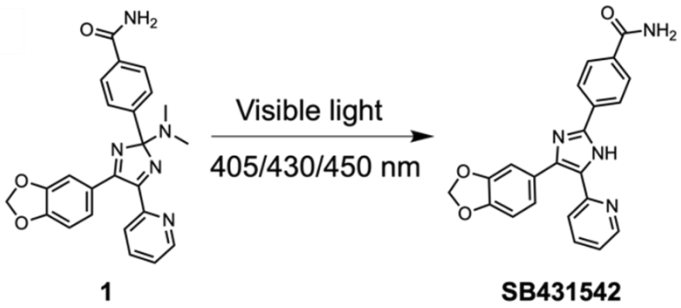

Scheme 4. The uncaging of **1** to form **SB431542** upon visible light irradiation.

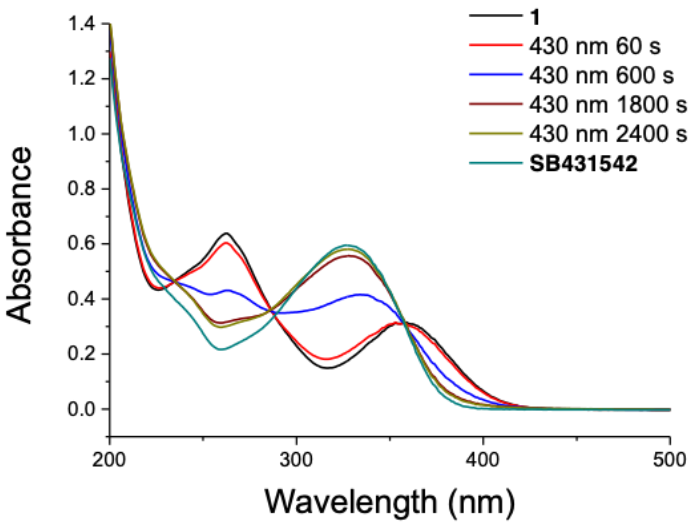

Figure 9. UV-visible absorption spectra of **1** recorded in acetonitrile:water (1:1) mixture upon irradiating with 430 nm light for different time periods and UV-visible absorption spectrum of **SB431542**.

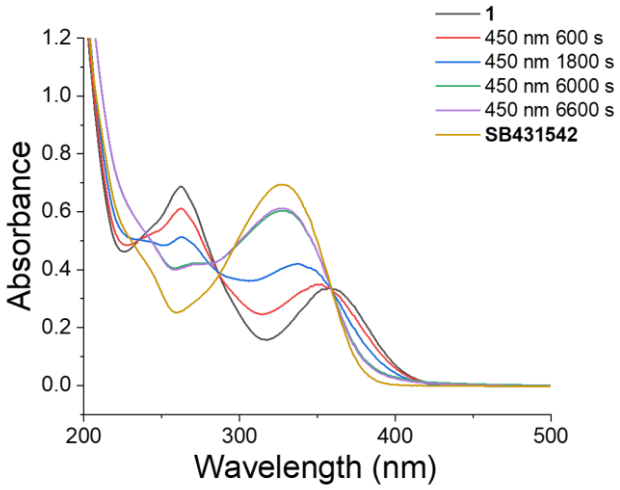

Figure 10. UV-visible absorption spectra of **1** recorded in acetonitrile:water (1:1) mixture upon irradiating with 450 nm light for different time periods and UV-visible absorption spectrum of **SB431542**.

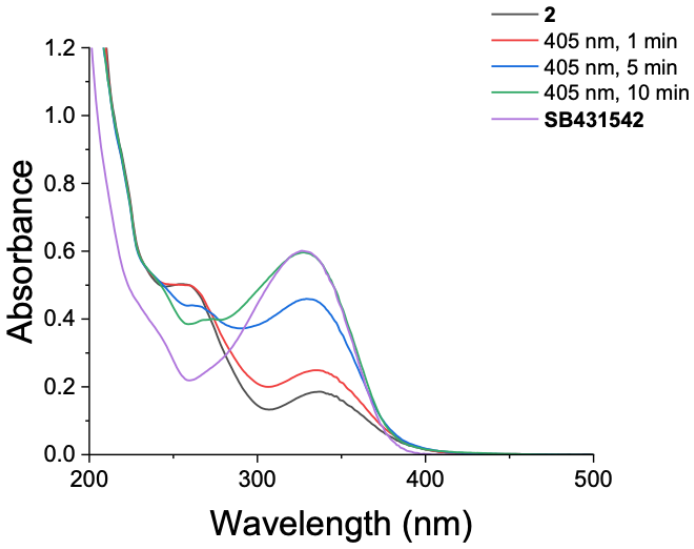

Figure 11. UV-visible absorption spectra of **2** recorded in acetonitrile:water (1:1) mixture upon irradiating with 405 nm light for different time periods and UV-visible absorption spectrum of **SB431542**.

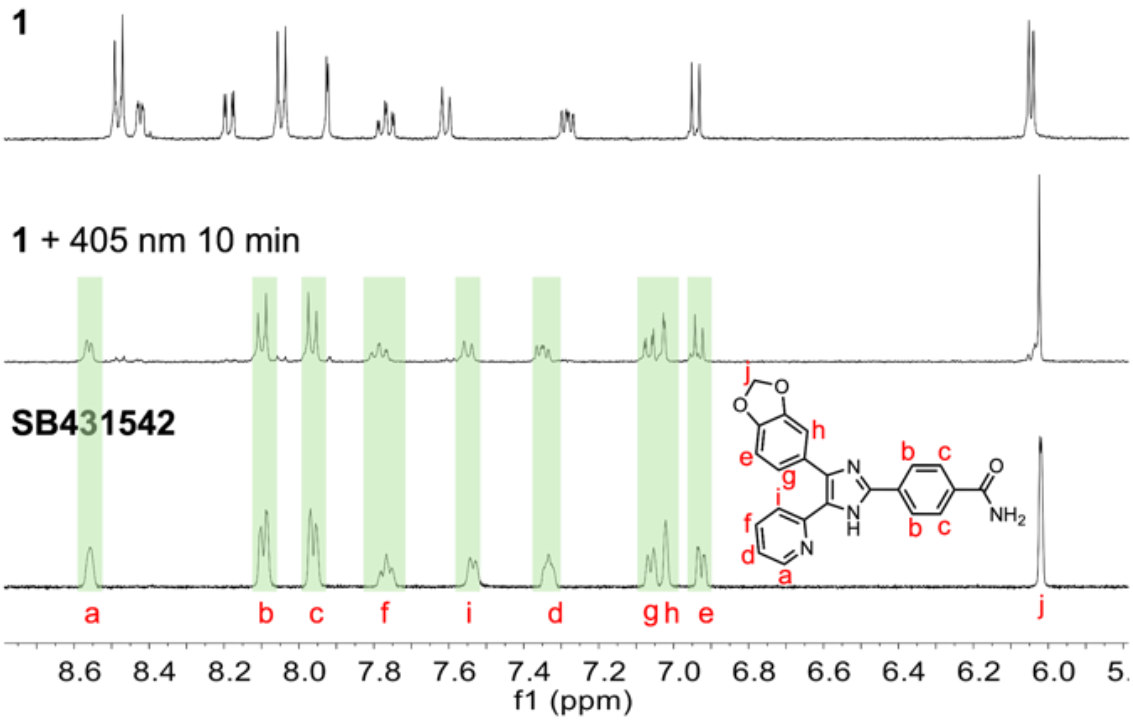

Figure 12. ^{1}H NMR spectra of SB431542, 1, and 1 after irradiation with 405 nm light for 10 min (measured in the 1:1 mixture of CD_3CN and D_2O).

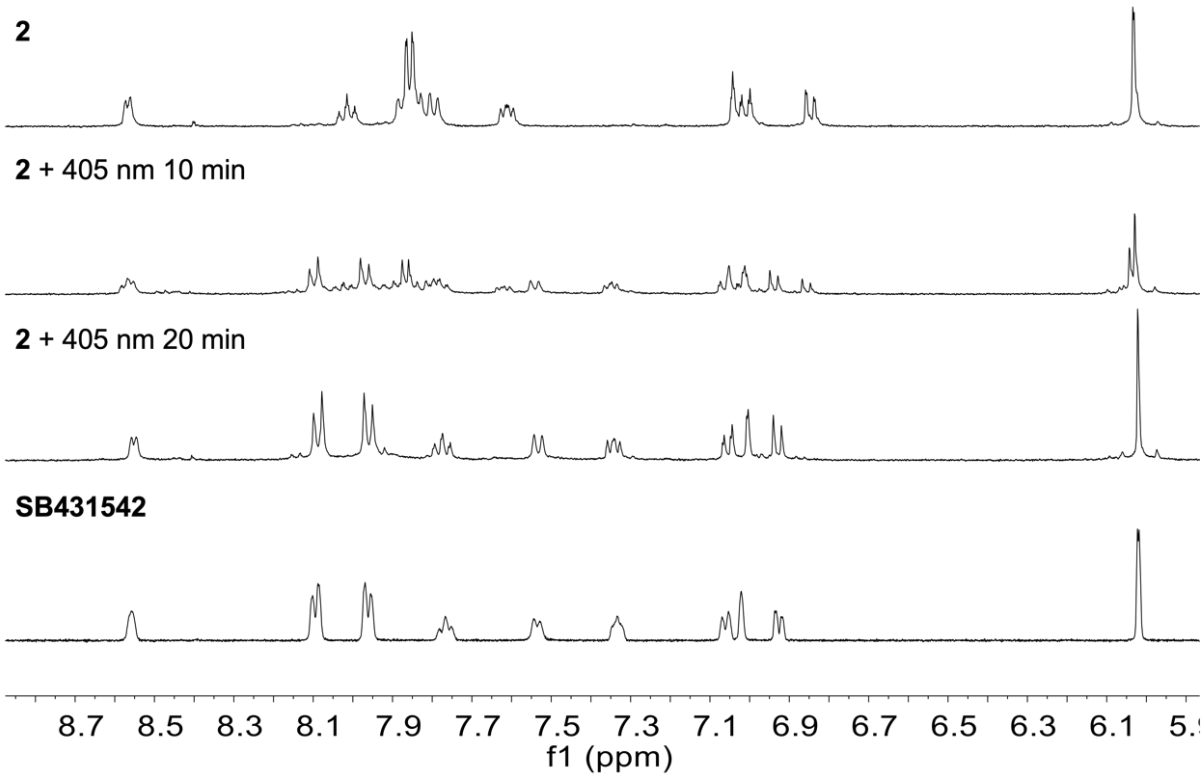

Figure 13. ^{1}H NMR spectra of **SB431542**, **2**, and **2** after irradiated with 405 nm light for 10 and 20 minutes recorded in acetonitrile-d_3 and D_2O (1:1) mixture.

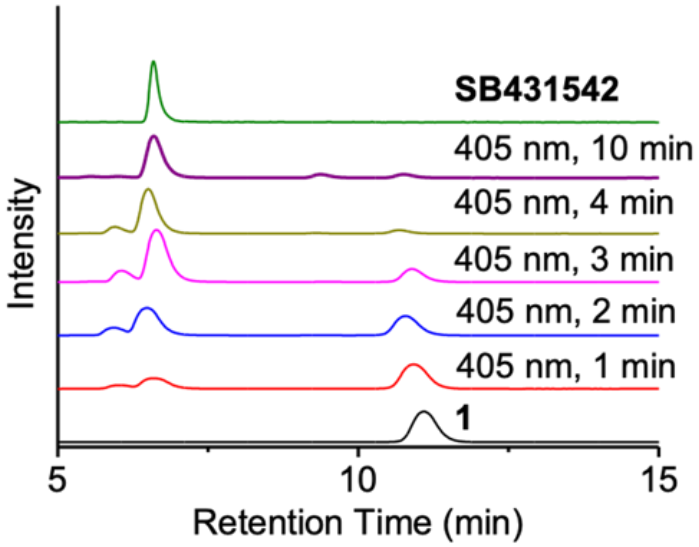

Figure 14. HPLC chromatograms of 1 after irradiation with 405 nm light for different time periods.

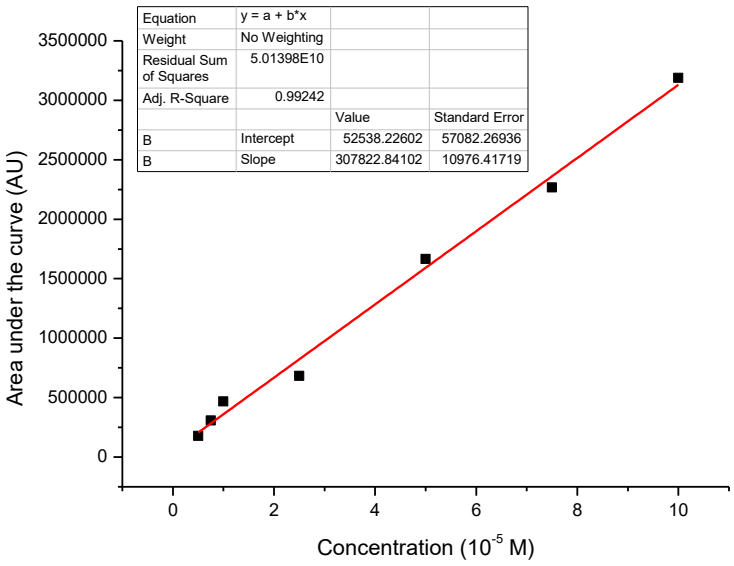

Figure 15. Calibration curve for **1**.

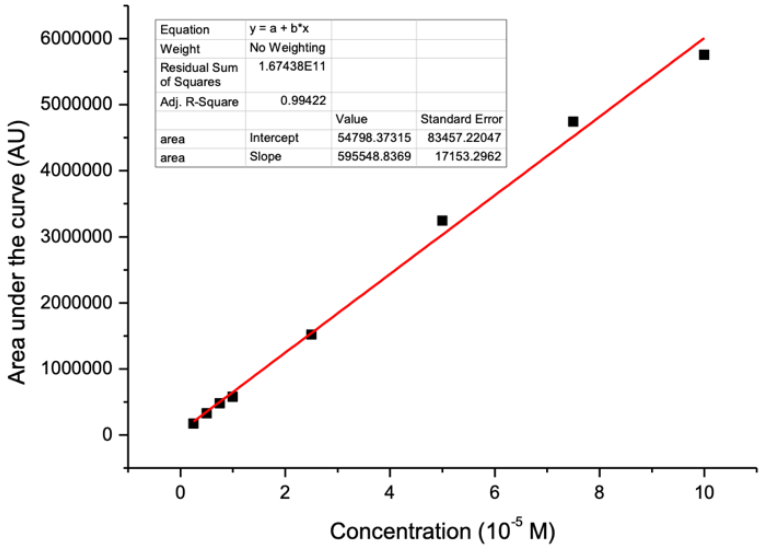

Figure 16. Calibration curve for **SB431542**.

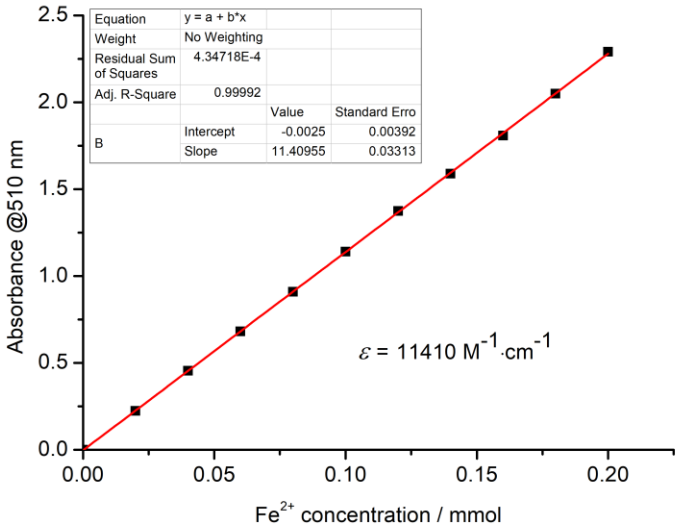

Figure 17. Calibration chart plotting the concentration of Fe^{2+} ions against the absorbance at 510 nm.[3] This graph was utilized to determine the extinction coefficient of the ferrioxalate-phenanthroline complex, also known as ferroin, at 510 nm. The calibration solutions were prepared by diluting a commercially available 0.1 mol/L $FeSO_4$ solution (purchased from Hayashi Pure Chemical, Lot No T211109001) in a sodium acetate buffer containing phenanthroline (0.1 wt%, 300 µL).

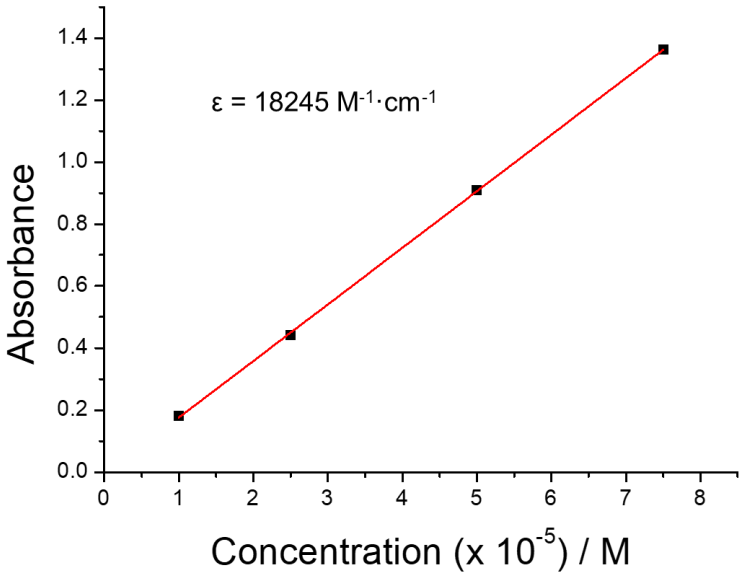

Figure 18. Graph of varying concentration of **1** against absorbance at λ_{max} (262 nm, red line). Extinction coefficient of **1** was calculated from the slope of a linear fit.

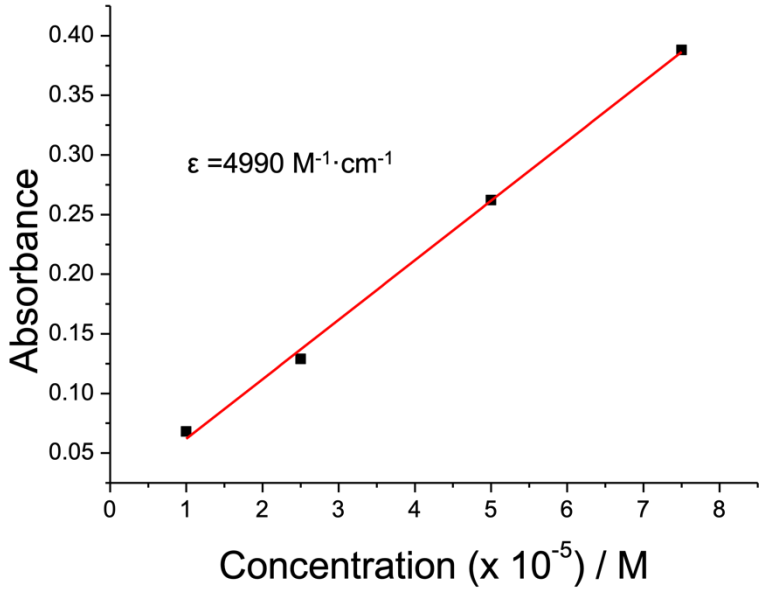

Figure S19. Graph of varying concentration of **SB431542** against absorbance at λ = 262 nm (red line). Extinction coefficient of **SB431542** was calculated from the slope of a linear fit.

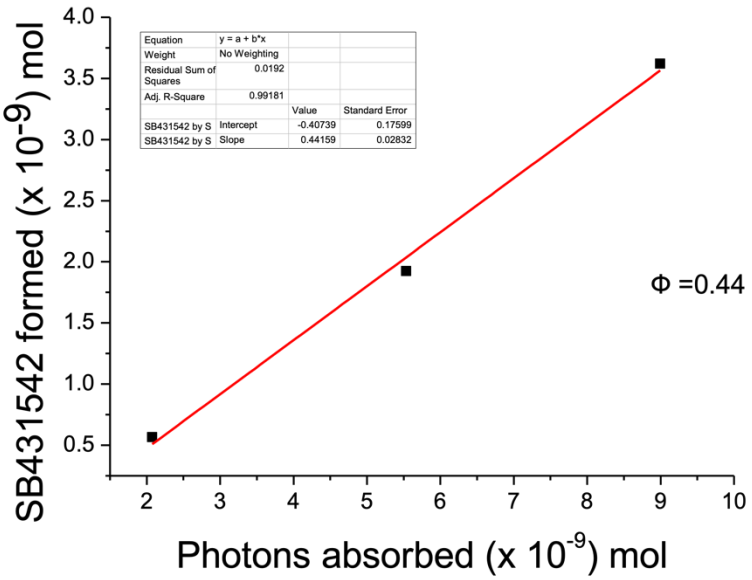

Figure 20. Graph showing the amount of **SB431542** formed under different light intensity (0.15–0.56 mW/cm^2). Photons absorbed by **1** were calculated and the slope of the graph gives the quantum yield for the photocleavage reaction of **1**.

ε_1	$\varepsilon_{SB431542}$	Φ
18245	4990	0.44

Table 1. Table showing the calculated values and photocleavage reaction quantum yield of **1** at 405 nm light irradiation.

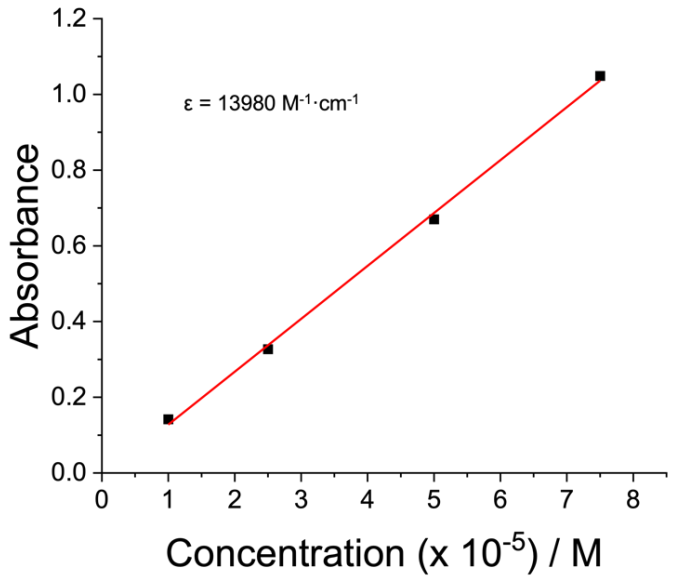

Figure 21. Graph of varying concentration of **2** against absorbance at λ_{max} (255 nm, red line). Extinction coefficient of **2** was calculated from the slope of a linear fit.

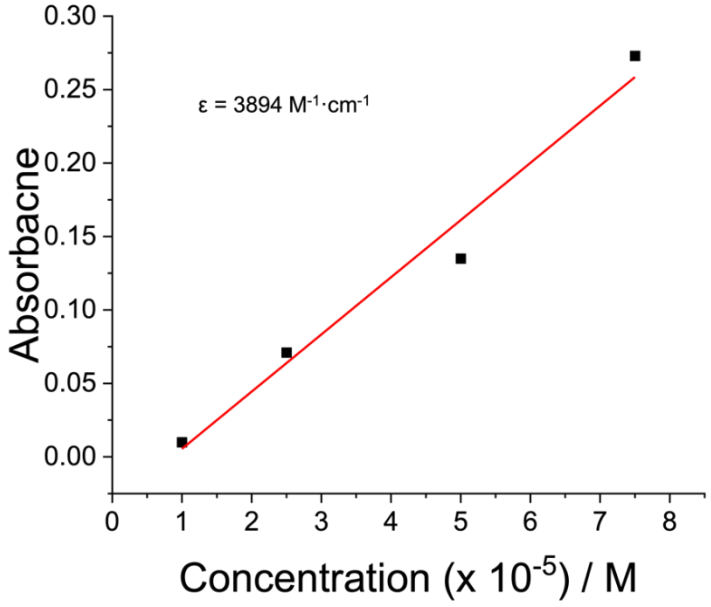

Figure 22. Graph of varying concentration of **SB431542** against absorbance at λ = 255 nm (red line). Extinction coefficient of **SB431542** was calculated from the slope of a linear fit.

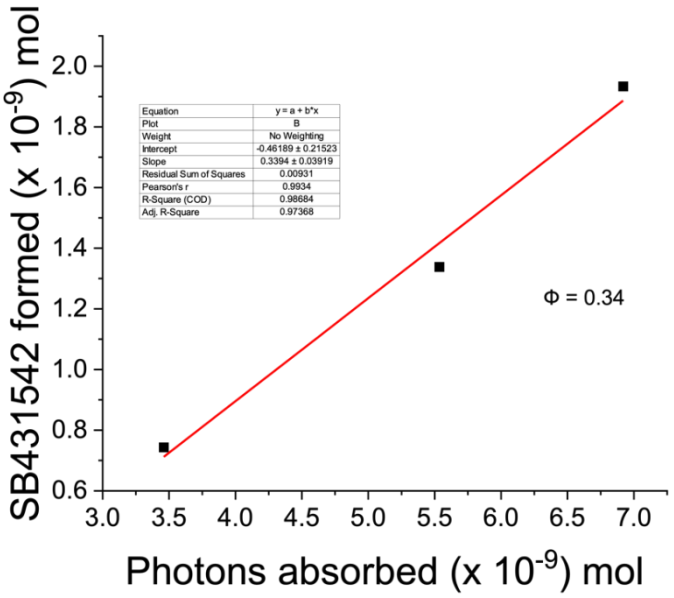

Figure 23. Graph showing the amount of **SB431542** formed under different light intensity (0.15–0.56 mW/cm^2). Photons absorbed by **2** were calculated and the slope of the graph gives the quantum yield for the photocleavage reaction of **2**.

ε_1	$\varepsilon_{SB431542}$	Φ
13980	3894	0.34

Table 2. Table showing the calculated values and photocleavage reaction quantum yield of **2** at 405 nm light irradiation.

2.2 Immunoblotting Analysis

To evaluate the effect of **1** on TGF- β signaling, I investigated TGF- β -dependent activation of Smad2, a major downstream molecule of TGF- β pathway,[23] using breast cancer cells MDA-MB-231 and glioblastoma cells KMG. I employed immunoblot analysis to assess Smad2 phosphorylation. These cells were treated with **1** or **SB431542** as a control. **SB431542** effectively inhibited the TGF-β-dependent phosphorylation of Smad2 in both cell types (Figure 24; lane 3). Similarly, **1** suppressed the phosphorylation of Smad2 only upon light irradiation (Figure 24; lanes 5 and 6). These results demonstrate that at 10 *m*M concentration, **1** has minimal inhibition activity against Smad2 phosphorylation in TGF-b signaling pathway. However, upon irradiation **1** produces **SB431542**, resulting in inhibition of TGF-b signaling.

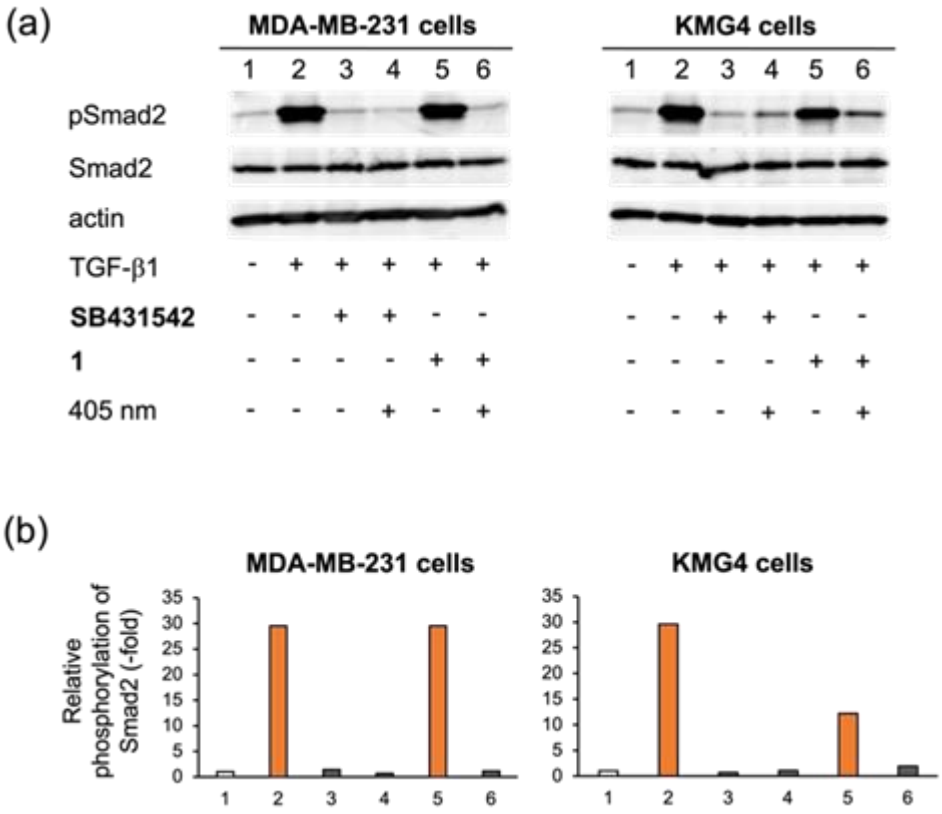

Figure 24. (a) Protein and phosphorylation levels of Smad2 upon treating with **1**. MDA-MB-231 (left) and KMG4 cells (right) were treated with 10 μM of **SB431542** (lanes 3 and 4) and 10 μM of **1** (lanes 5 and 6) in the presence or absence of 405 nm light irradiation, and TGF-β-dependent phosphorylation of Smad2 was examined by immunoblotting. Actin was used as a loading control. (b) Relative phosphorylation levels of Smad2 are displayed in the graph. The numbers below the graph indicate the same treatment as shown in (a) above.

2.3 Wound Healing Assay

After confirming the generation of the authentic TGF-β R1 inhibitor, **SB431542**, from **1** and **2** upon visible light irradiation, and understanding **1**'s function in regulating the TGF-β signaling pathway through light irradiation, our goal was to validate the applicability of **1** and **2** for photo-regulation of cellular movement. In TGF-β signaling, activated Smad complex can induce the expression of several transcription factors in the nucleus to promote fibroblast activation that plays a critical role in wound healing. It has been reported that **SB431542** effectively blocks TGF-β–induced cell migration in a wound healing experiment.[17, 24, 25] For our study, I conducted a wound healing assay[26] using **1**, a photoswitchable inhibitor for the TGF-β signaling pathway, both in the presence and absence of light with the breast carcinoma cell line, MDA-MB231.

Initially, I determined the EC_{50} values of **SB431542**, **1**, and **2** by performing the wound healing assay at different concentrations and the EC_{50} values were found to be 3.3, 23.1, and 30.9 μM, respectively (Figure 25-27). In the control experiment performed with dimethylsulfoxide (DMSO), slight wound recovery was observed within 24 h (gap reduction of approximately 35 μm, Figure 28a(i)). However, cells treated with TGF-β1 (3 ng/mL) showed more significant wound recovery (gap reduction of approximately 85 μm, Figure 28a(ii)). Irradiation of TGF-β1–treated cells with 405 nm light for 3 min at 15.5 mW/cm^2 intensity did not affect the wound healing process (Figure 28a(iii)). Cells treated with TGF-β1 and **SB431542** (10 *m*M) showed approximately equivalent wound recovery to that in the control experiment, indicating the inhibitory effect of **SB431542** on TGF-β R1 (Figure 28a(iv)). Cells treated with TGF-β1 and **1** (10 *m*M) exhibited almost equivalent wound recovery to that of cells treated solely with TGF-β1, suggesting the non-inhibitory effect of **1** (Figure 28a(v)). However, irradiation of cells treated with TGF-β1 and **1** with 405 nm light for 3 min resulted in equivalent wound recovery to that of cells treated with TGF-β1 and **SB431542**, indicating photocleavage of **1** to generate **SB431542** in the cellular environment (Figure 28a(vi)).

The results of the wound healing assay with **1**, conducted as single set of experiment, are summarized in Figure 28b. A similar photoresponsive wound healing was observed with

2 (Figure 29). The same trend is reproduced with two other independent sets of experiment for both **1** and **2** (Figure 30).

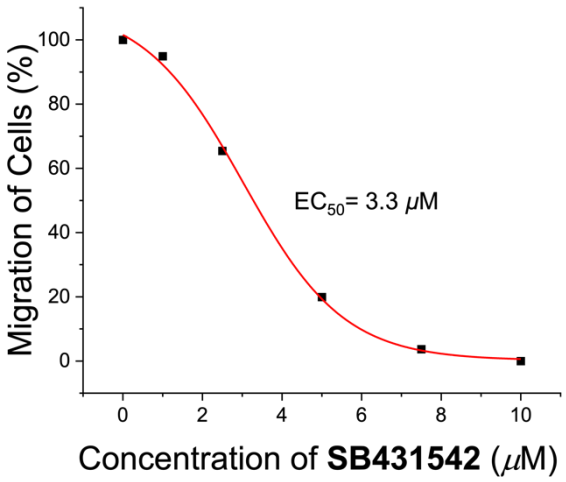

Figure S25. Graph of concentration dependent percentage cell migration for **SB431542**.

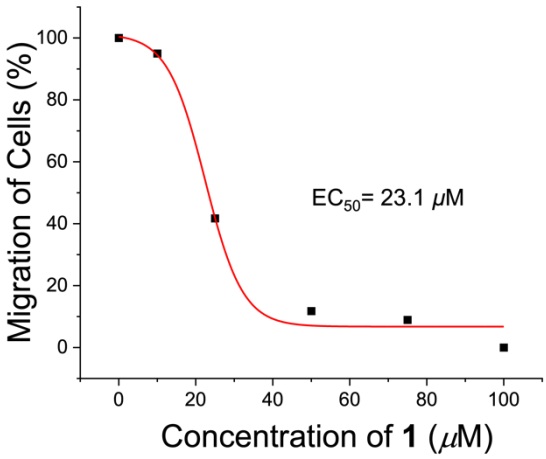

Figure S26. Graph of concentration dependent percentage cell migration for the compound **1**.

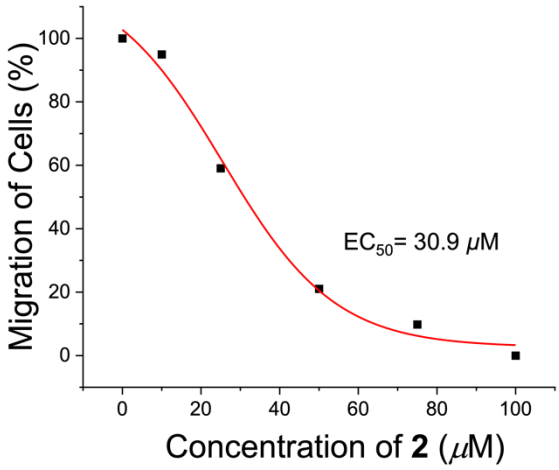

Figure 27. Graph of concentration dependent percentage cell migration for the compound **2**.

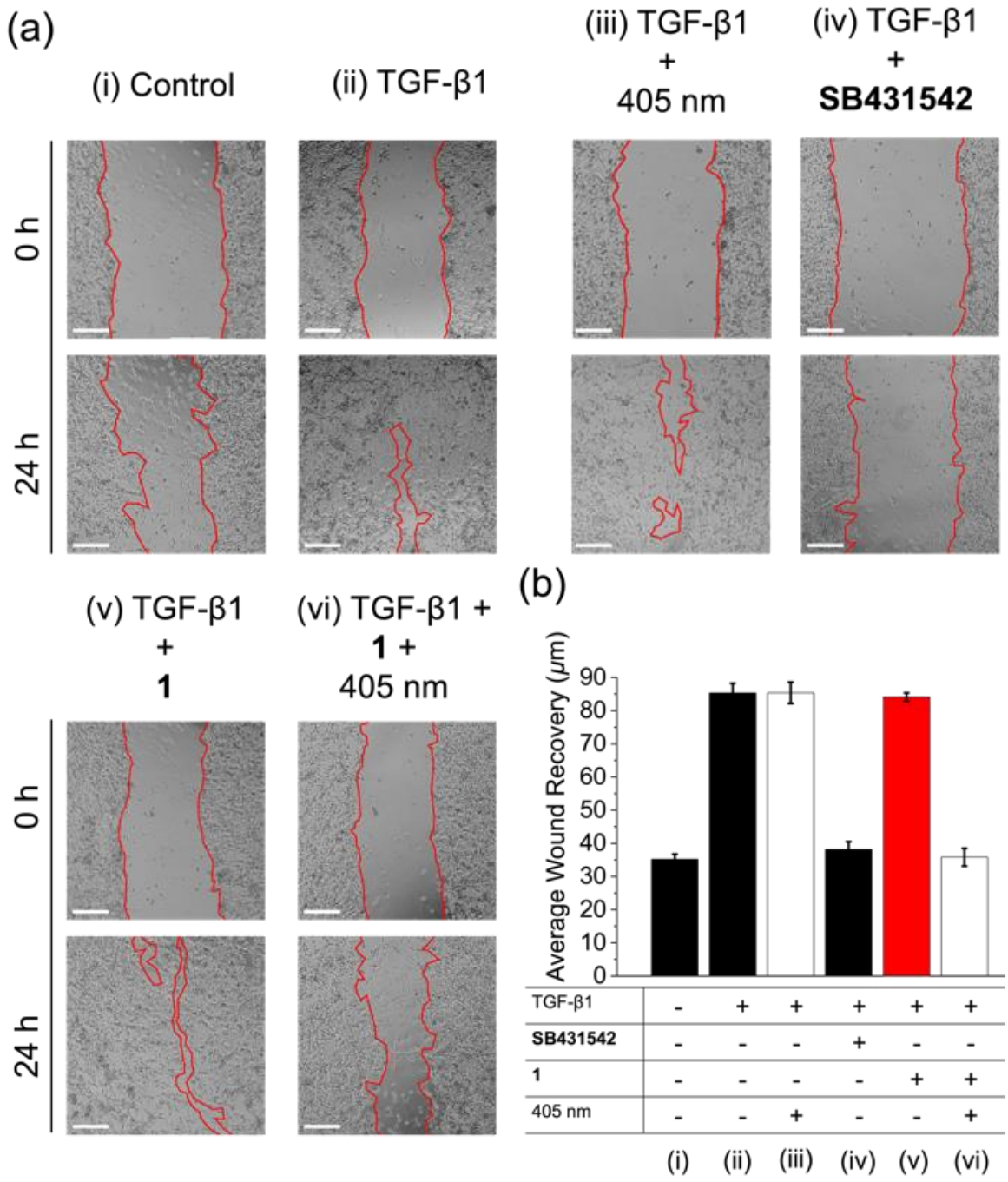

Figure 28. Wound healing assays performed with MDA-MB-231 cells. (a) Representative images of wound recovery upon different treatments at 0 and 24 h. Scale bar = 100 μm (b) Average wound recovery of MDA-MB-231 cells under different conditions after 24 h (single set of experiments). Error bars represent the standard deviation for measurements of three different areas of the wound in a single well.

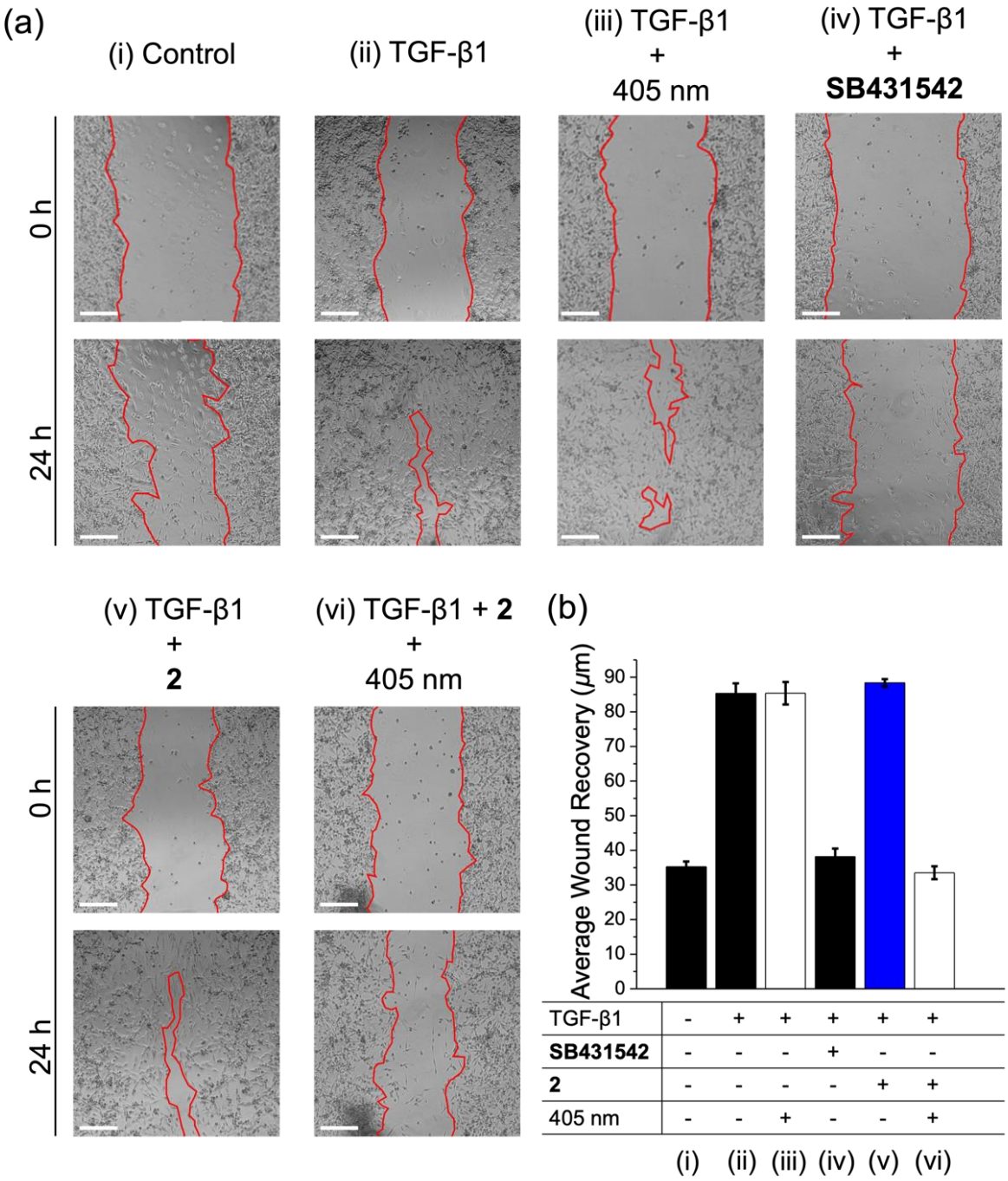

Figure 29. Wound healing experiments on MDA-MB-231 cells using **2**. (a) Images of MDA-MB-231 cells upon different treatments at 0 h and after 24 hours. Scale bar = 100 μm (b) Average wound recovery of MDA-MB-231 cells at different conditions after 24 hours for the single set of experiments. Error bars represent the standard deviations for three different areas of the wound in a single well.

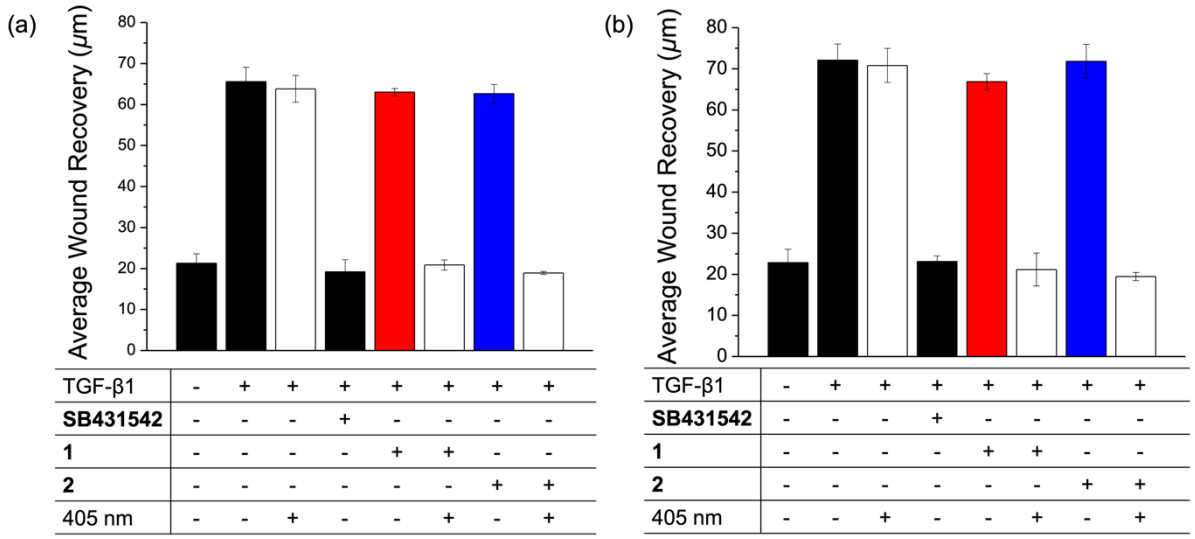

Figure 30. (a) and (b) Results of wound healing assays performed on MDA-MB-231 cells obtained from two different sets of experiments. Average wound recovery of MDA-MB-231 cells at different conditions after 24 hours is presented. Error bars represent the standard deviations for three different areas of the wound in a single well.

2.4 Spatiotemporal Regulation

To demonstrate the effectiveness of our strategy in achieving localized activity against cancer cells by selectively inhibiting TGF-β R1 at a specific region of interest while maintaining its activity in the surrounding region, I created two wounds in a single well, treated cells with TGF-β1, **SB431542**, and **1**, and subjected one wound to visible light irradiation but not the other. Figure 4a illustrates the experimental setup used for the spatiotemporal regulation experiments, wherein the well was covered with aluminum foil, leaving only one wound exposed, and the well was irradiated with 405 nm light at an intensity of approximately 0.1 mW/cm^2 for 24 h (Figure 31b). Cell migration in the irradiated and non-irradiated wounds was recorded (Figure 32).

As expected, cells treated solely with DMSO or TGF-β1 and those treated with TGF-β1 and **SB431542** did not exhibit any differences in the wound healing process at 405 nm-light- exposed and covered areas (Figure 32(i–vi)). However, cells treated with TGF-β1 and **1** exhibited clear differences in the wound healing process at the exposed (Figure 32(viii)) and covered (Figure 32(vii)) areas. The average wound recovery under various exposure conditions is summarized in Figure 33. Similar results were obtained with **2** (Figure 34). The same trend is reproduced with another independent experiment (Figure 35).

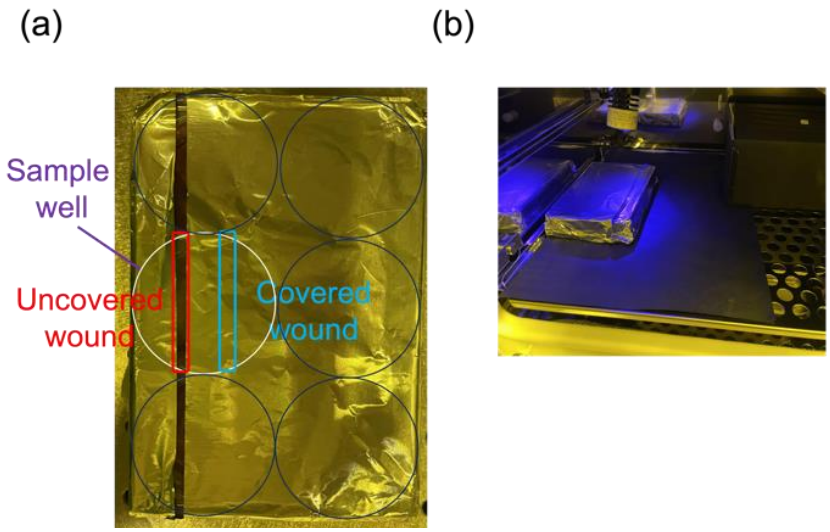

Figure 31. Spatiotemporal regulation of wound healing with MDA-MB-231 cells. (a) Experimental arrangement of spatiotemporal regulation experiments. (b) Irradiation setup used to irradiate samples for 24 h inside the incubator.

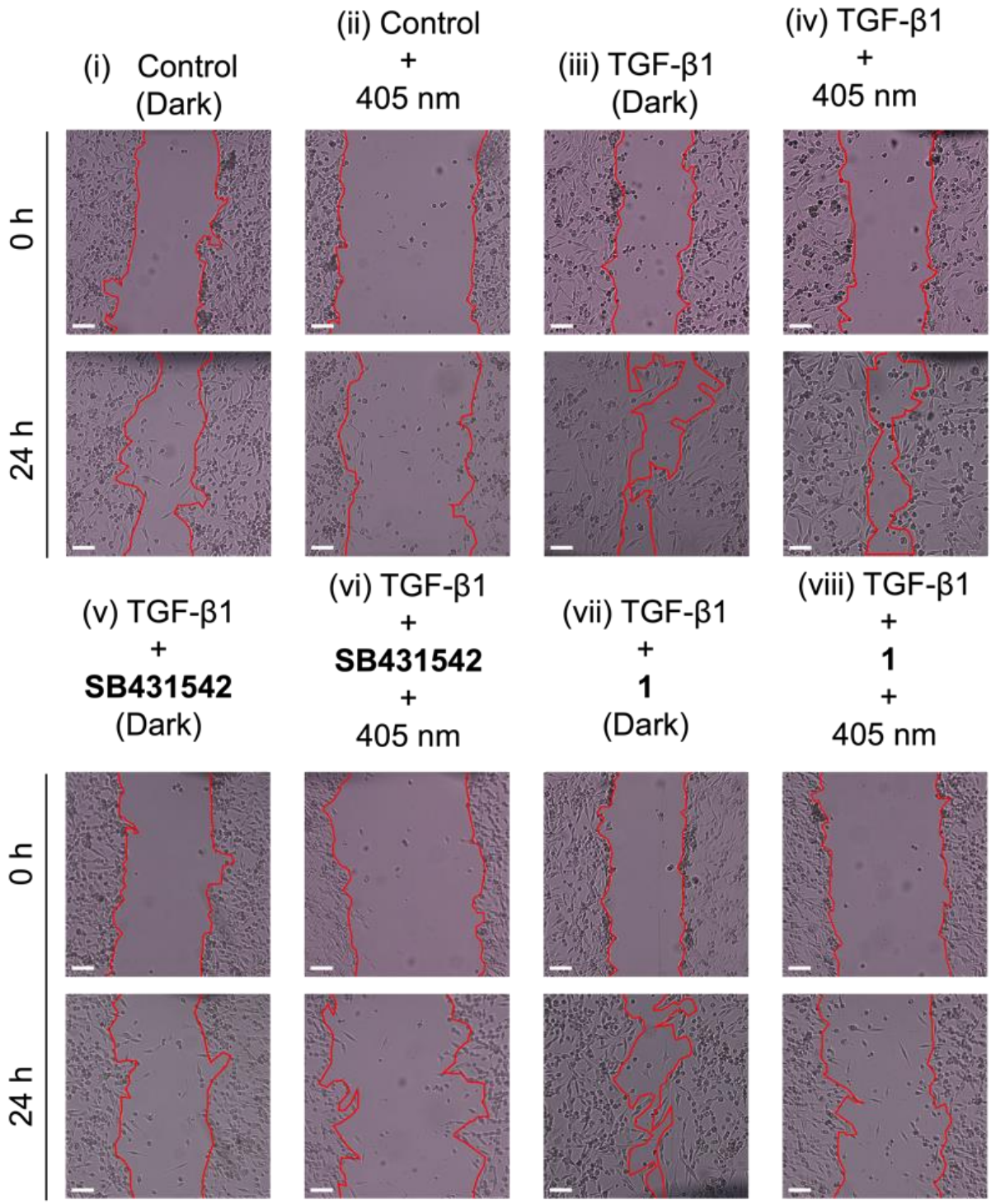

Figure 32. Representative images of cells upon different treatments at 0 and 24 h. Scale bar = 100 μm.

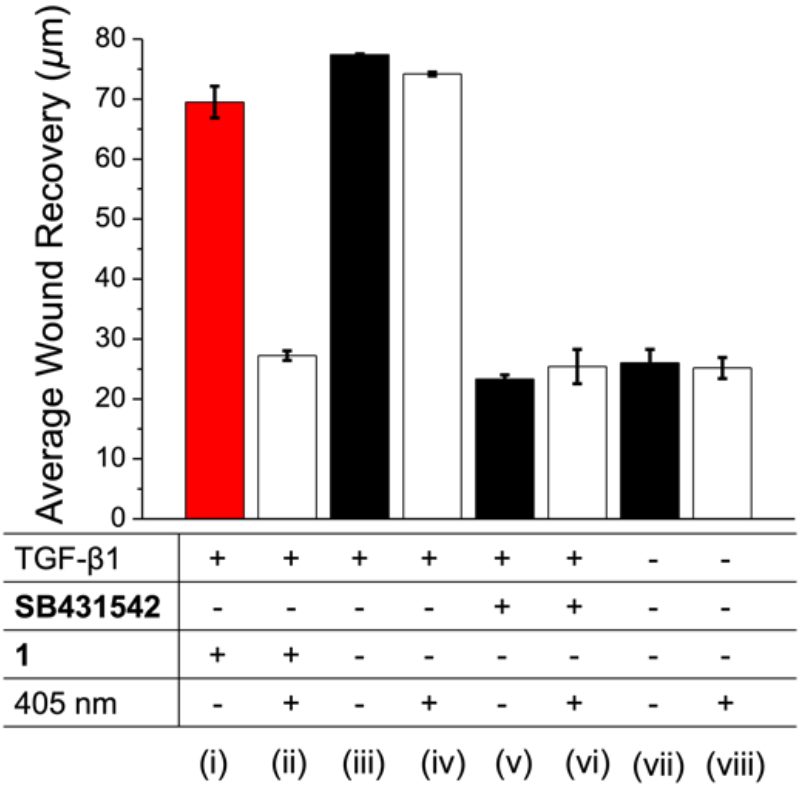

Figure 33. Average wound recovery of cells under different conditions after 24 h (single set of experiments). Error bars represent the standard deviation for measurements of three different areas of the wound created in a single well.

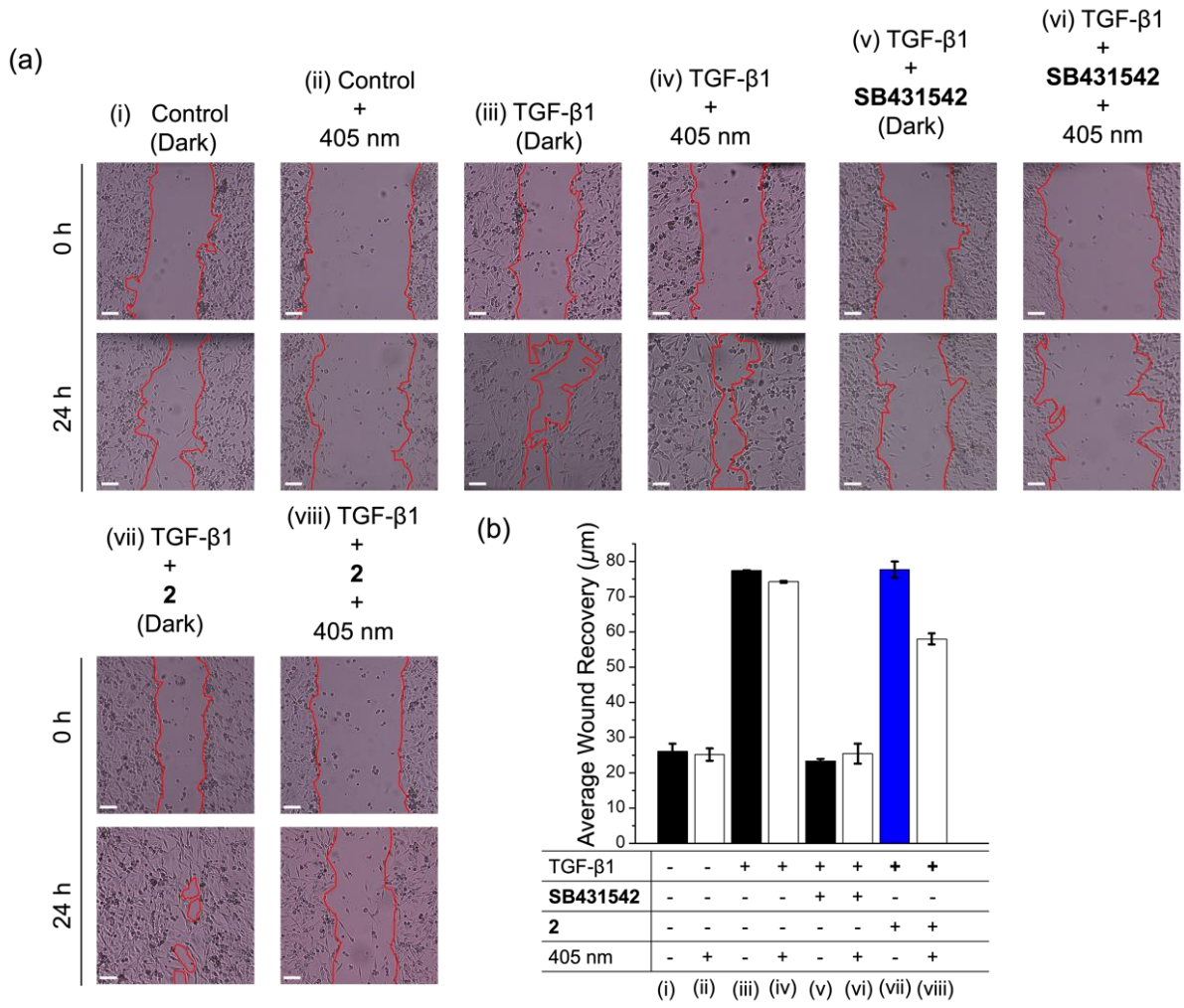

Figure 34. Spatiotemporal regulation of wound healing in MDA-MB-231 cells using **2**. (a) Images of MDA-MB-231 cells upon different treatments at 0 h and after 24 hours. Scale bar = 100 μm. (b) Average wound recovery of MDA-MB-231 cells at different conditions after 24 hours calculated based on single set of experiment. Error bars represent the standard deviations for three different areas of the wound in a single well.

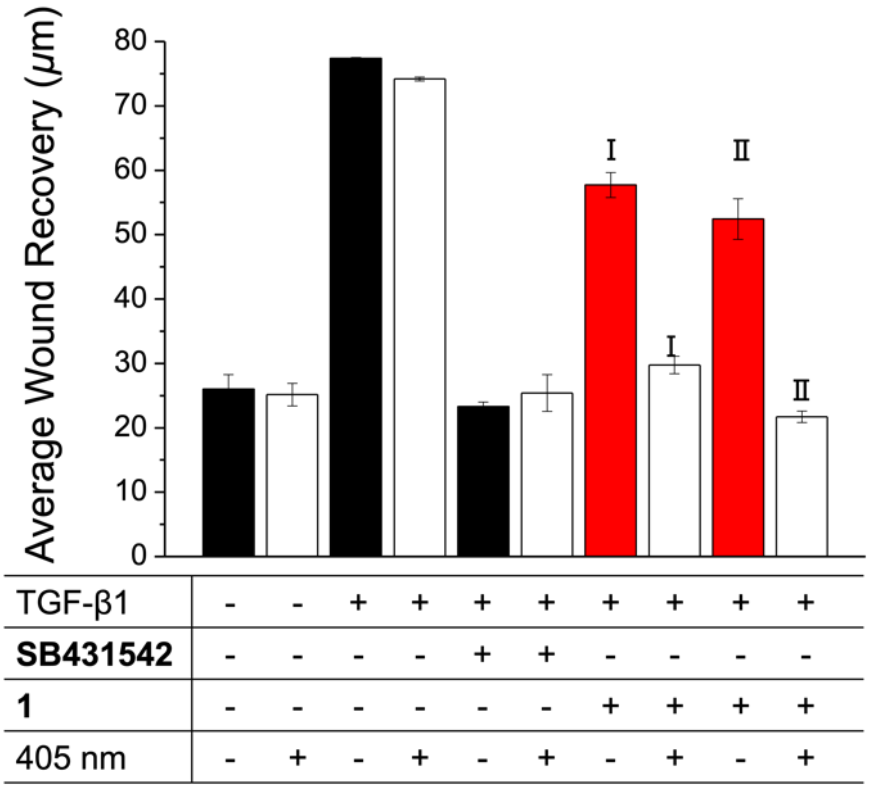

Figure 35. I and II are the results of spatiotemporal regulation of wound healing process in MDA-MB-231 cells using **1** obtained from two different sets of experiments. Average wound recovery of MDA-MB-231 cells at different conditions after 24 hours under dark and 405 nm light irradiation conditions is presented. Error bars represent the standard deviations for three different areas of the single wound in a single well.

2.5 Molecular Docking Studies

Molecular docking simulations were employed to assess the binding affinities of **1** and **2** with respect to the binding site of **SB431542** in TGF-β R1. The TGF-β R1 structure obtained from the Protein Data Bank (PDB ID: 3TZM)[27] served as the receptor model. Figure 36a–c presents the docked structures of the ligands in the **SB431542** binding site of TGF-β R1. The docking results revealed lower binding affinities for **1** and **2** compared to **SB431542** (Figure 36d). All ten different docking poses of each ligand are presented in the Supporting Information (Figure 37).

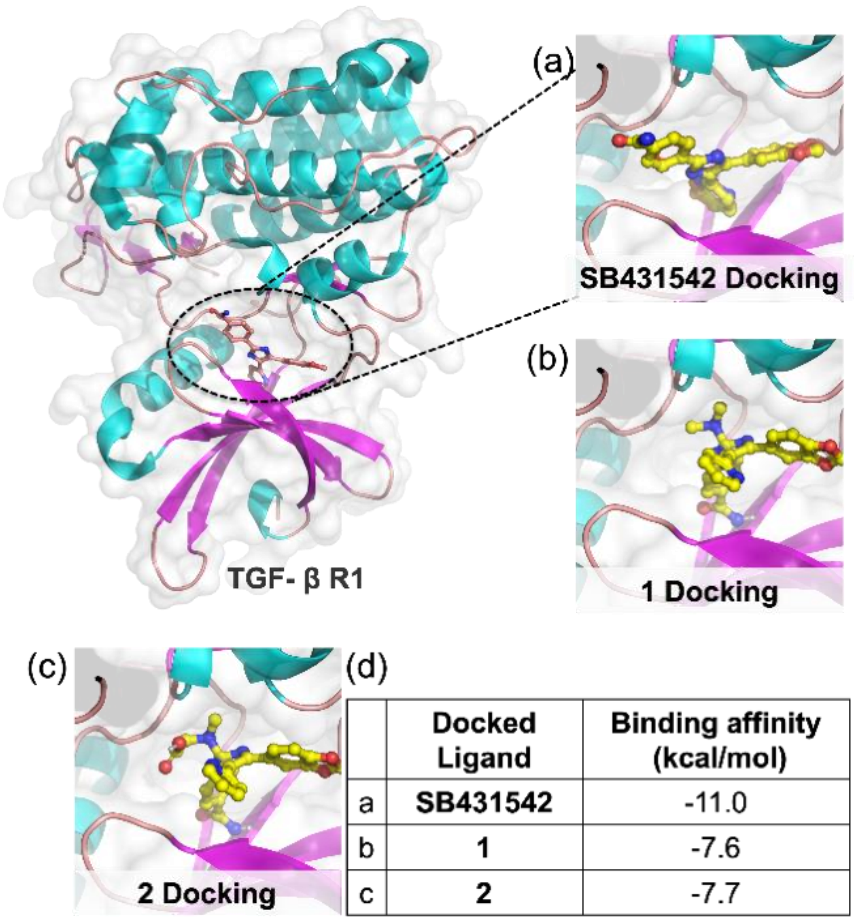

	Docked Ligand	Binding affinity (kcal/mol)
a	**SB431542**	-11.0
b	**1**	-7.6
c	**2**	-7.7

Figure 36. Docked ligands in the SB431542 binding site of TGF- β R1 (PDB: 3TZM). (a) Ligand SB431542 in the binding site of TGF- β R1 superimposed with docked SB431542. (b) Docked 1. (c) Docked 2. (d) Table presenting the binding affinities of docked ligands.

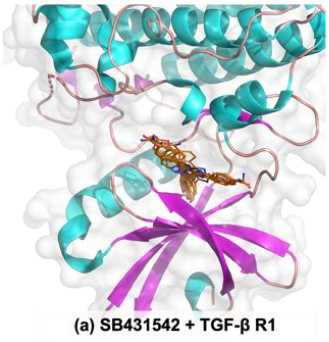

(a) SB431542 + TGF-β R1

Mode	Binding Affinity (kcal/mol)
1	**-11.04**
2	-10.8
3	-10.72
4	-10.65
5	-10.48
6	-10.19
7	-10.09
8	-9.885
9	-9.748
10	-9.731

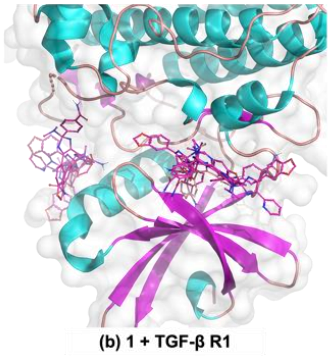

(b) 1 + TGF-β R1

Mode	Binding Affinity (kcal/mol)
1	**-8.083**
2	-7.602
3	-7.59
4	-7.496
5	-7.273
6	-7.254
7	-7.083
8	-7.04
9	-6.97
10	-6.94

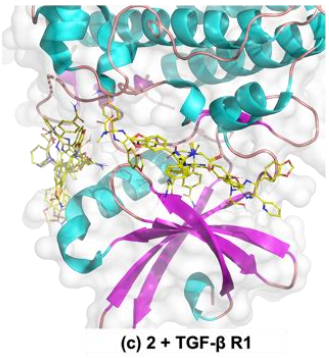

(c) 2 + TGF-β R1

Mode	Binding Affinity (kcal/mol)
1	**-7.732**
2	-7.695
3	-7.295
4	-7.293
5	-7.238
6	-7.153
7	-6.913
8	-6.88
9	-6.818
10	-6.801

Figure 37. Docked ligands in the **SB431542** binding site of TGF-β R1. (a) **SB431542** docked to TGF-β R1. (b) **1** docked to TGF-β R1. (c) **2** docked to TGF-β R1. In all the cases, the tables represent the binding affinity values corresponding to 10 different binding poses.

2.6 Attempts to Cage Different Types of Imidazoles

In our effort to evaluate the wider applicability of our caging technique, I applied it to various types of imidazole-based molecules. These included well-established drug molecules such as adezmapimod and neurodazine as well as other molecules like 2,4,5-triphenylimidazole (lophine), 2,5-diphenyl-1*H*-imidazole, 2-phenylbenzimidazole, and 2-phenylimidazole.

The adezmapimod (SB203580) molecule,[28] is an ATP-competitive inhibitor of p38 kinase. I obtained the dimethylamino adduct of adezmapimod (**3**) via ferrocyanide oxidation in the presence of dimethylamine (Scheme 5). However, the fluorine atom on the phenyl ring was unexpectedly substituted with the dimethylamino group. The C–N bond of **3** underwent photochemical cleavage upon exposure to 405 nm light, forming uncaged imidazole (**3a**) (Figures 38a and b, 39), the structure of which was confirmed by ^{1}H NMR and mass spectroscopy (Figure 40-41, 42, 43-44). The quantum yield of the photoreaction from **3** to **3a** at 405 nm estimated by the absorption spectra change was 0.72 (Figures 45-46, Tables 3).

Caging another imidazole-based drug molecule, neurodazine,[29] yielded **4** with a dimethylamino substitution (Scheme 6, Figures 47, 48, 49). Upon irradiation with 405 nm light the neurodazine was regenerated (Figures 50 and 51). Lophine the simplest triarylimidazole, is known for its bioactivity.[30] Therefore, I aimed to cage lophine, resulting in the formation of **5** with a dimethylamino substitution (Scheme 7, Figures 52, 53, and 54). Upon exposure to 405 nm light, **5** regenerated lophine (Figures 55 and 56). The quantum yield of the photoreaction from **5** to lophine at 405 nm, estimated by the absorption spectra change, was 0.75 (Figures 57-59, Tables 4). However, attempts to synthesize dimethylamino adducts of 2,5-diphenyl-1*H*-imidazole, 2-phenylbenzimidazole, and 2-phenylimidazole using oxidizing agents like $K_3[Fe(CN)_6]$ and PbO_2 were unsuccessful.

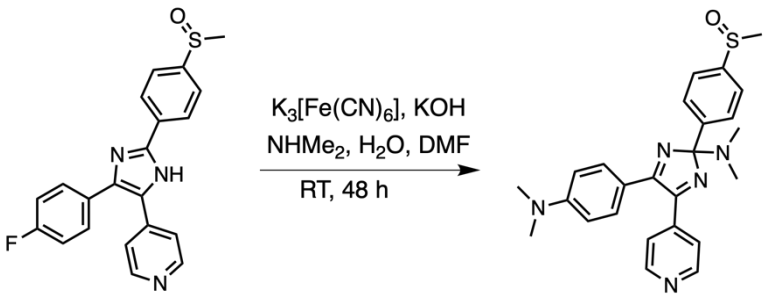

Scheme 5. Synthetic scheme for **3**.

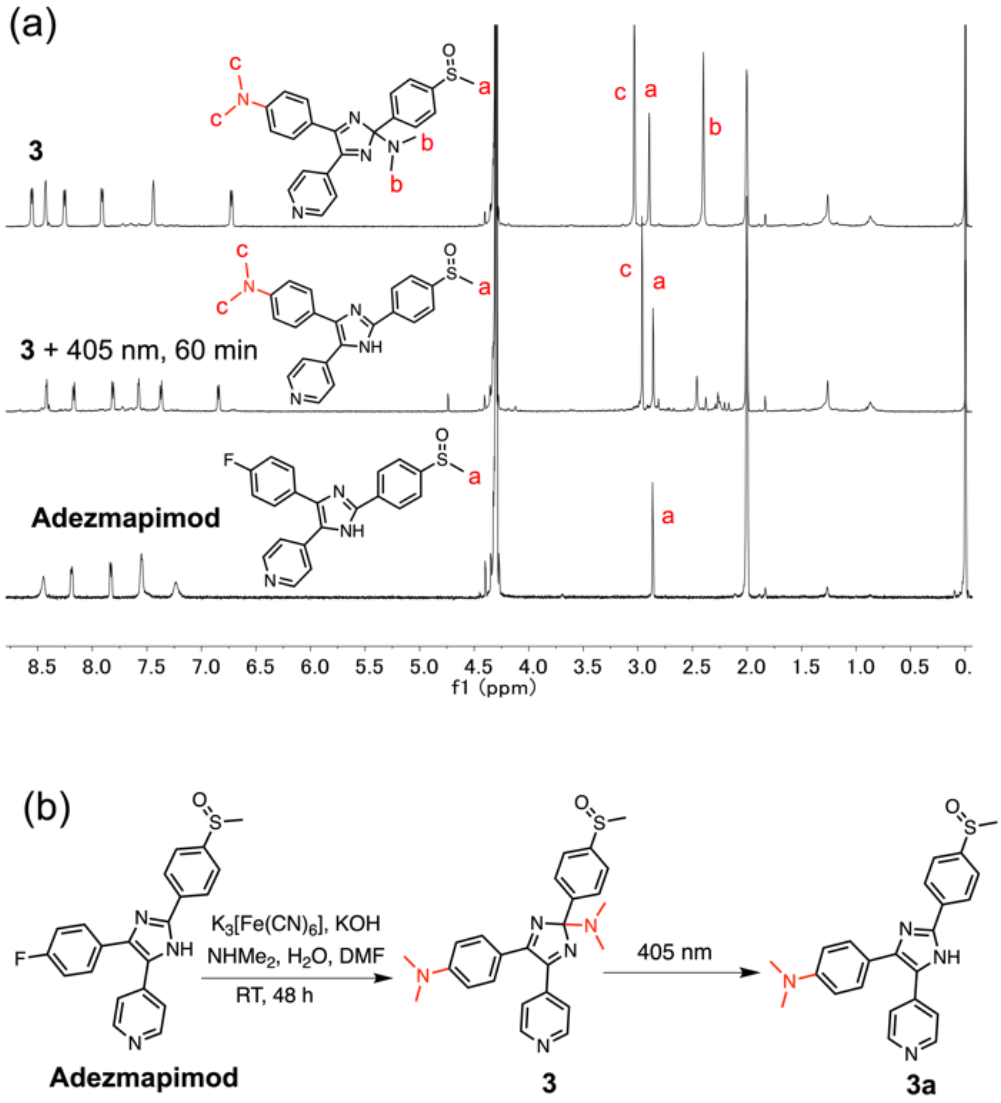

Figure 38. (a) ^{1}H NMR spectra of adezmapimod, **3**, and **3** after irradiation with 405 nm light for 60 min. (b) Scheme representing the formation of **3** and its photochemical reaction leading to the formation of **3a**.

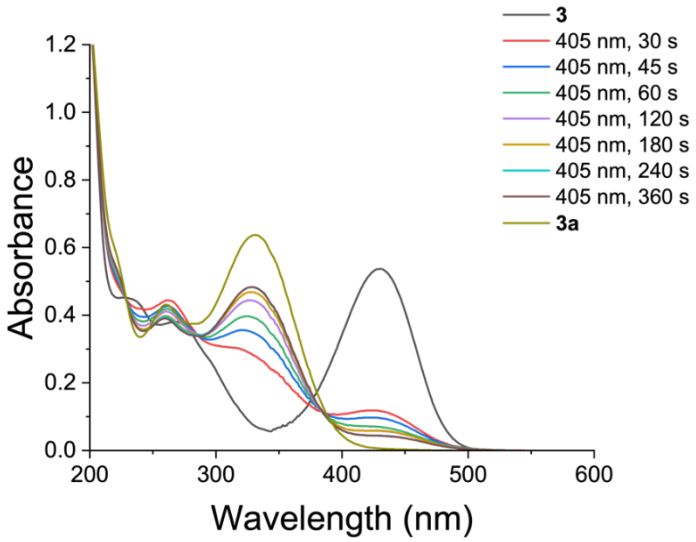

Figure 39. UV-visible absorption spectra of **3** recorded in acetonitrile:water (1:1) mixture upon irradiating with 430 nm light for different time periods and UV-visible absorption spectrum of **3a**.

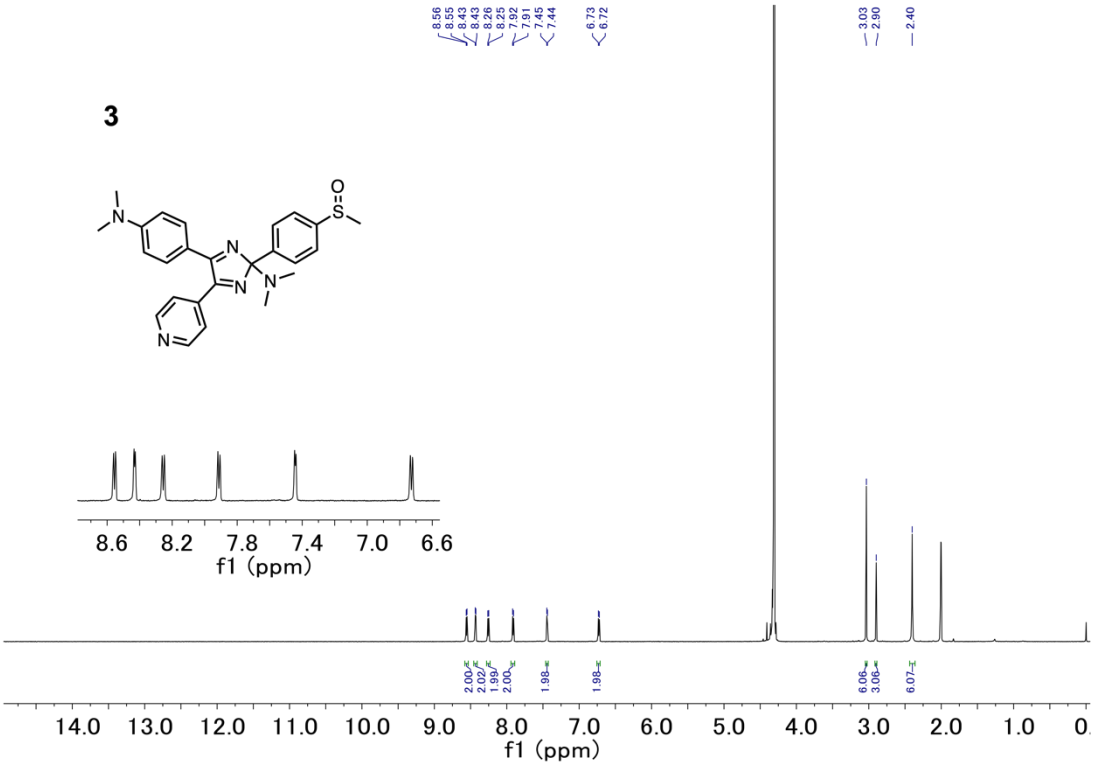

Figure 40. ^{1}H NMR spectrum of **3** recorded in acetonitrile-d_3 and D_2O (1:1) mixture.

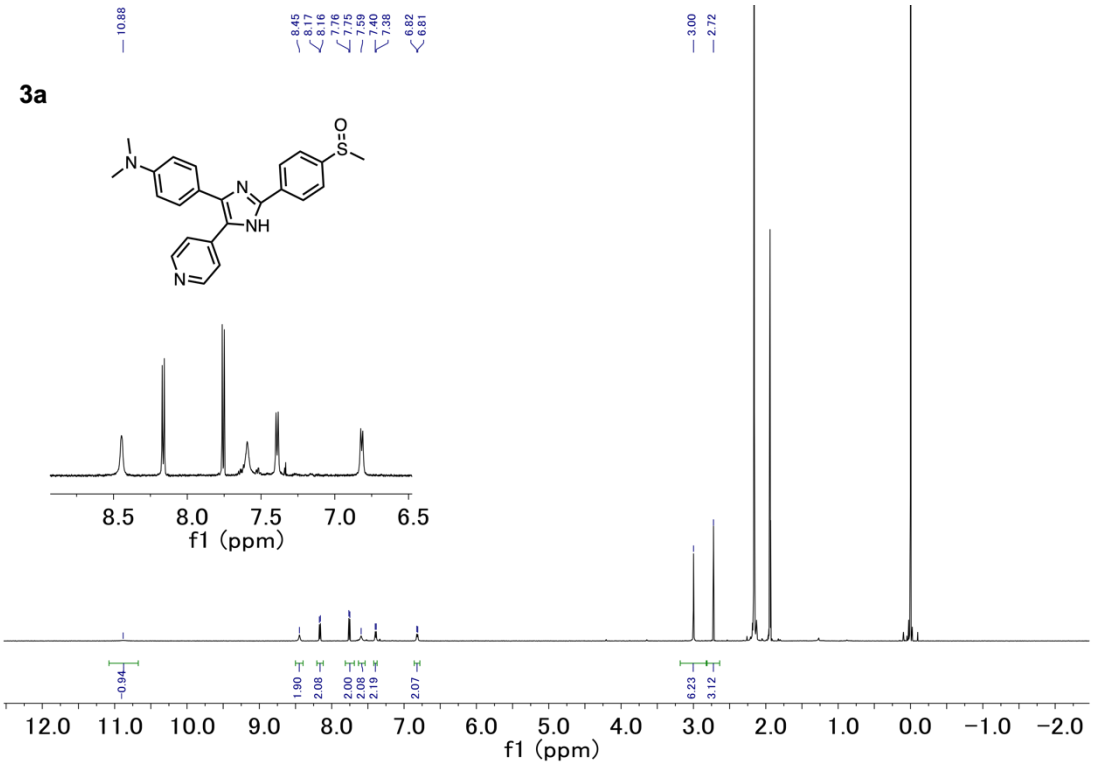

Figure 41. ^{1}H NMR spectrum of **3a** recorded in acetonitrile-d_3.

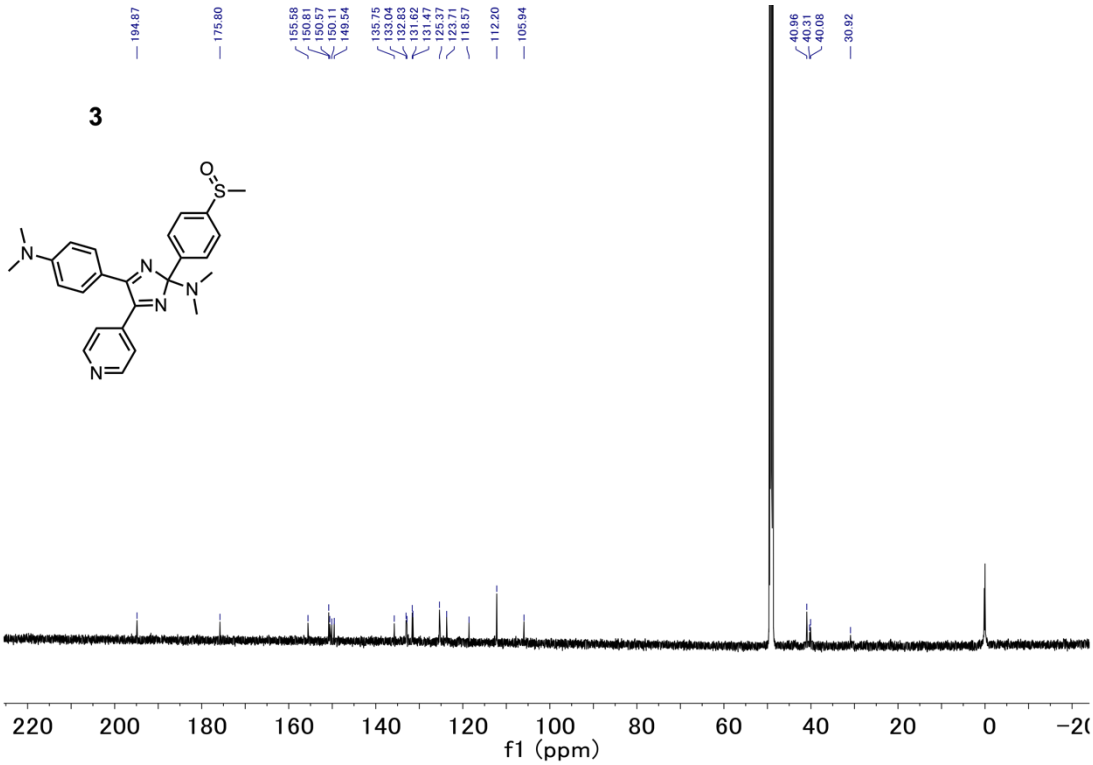

Figure 42. ^{13}C NMR spectrum of **3** recorded in CD_3OD.

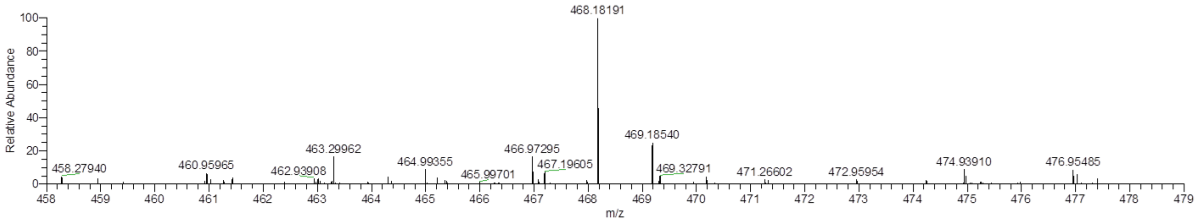

Figure 43. High resolution mass spectra (ESI) of **3** - m/z $[M+Na]^+$ calculated for $C_{25}H_{27}N_5OS$: 468.18340, found: 468.18191.

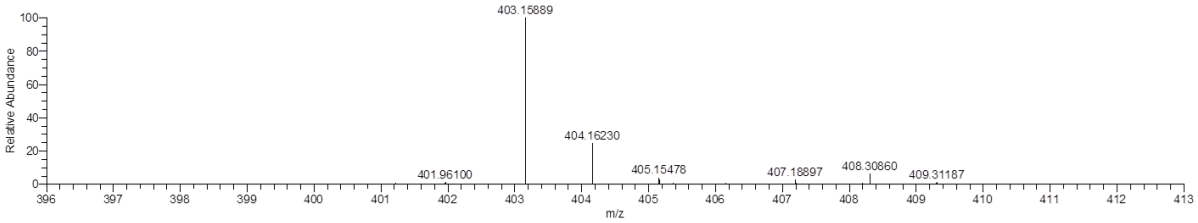

Figure 44. High resolution mass spectra (ESI) of **3a** - m/z $[M+H]^+$ calculated for $C_{23}H_{22}N_4OS$: 403.15926, found: 403.15889.

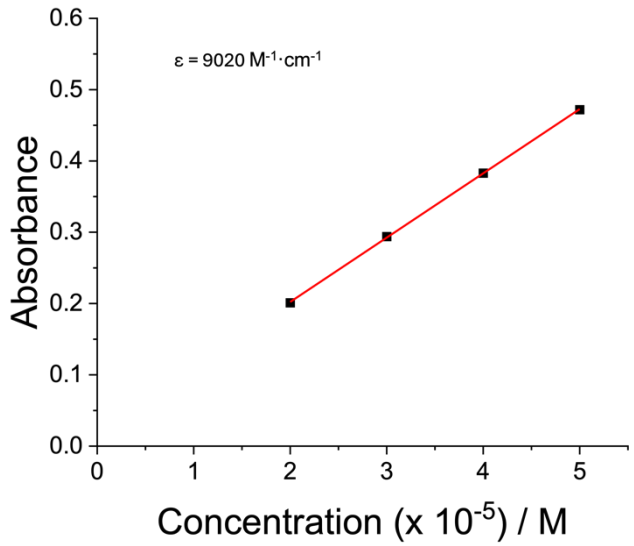

Figure 45. Graph of varying concentration of **3** against absorbance at λ_{max} (430 nm, red line). Extinction coefficient of **3** was calculated from the slope of a linear fit.

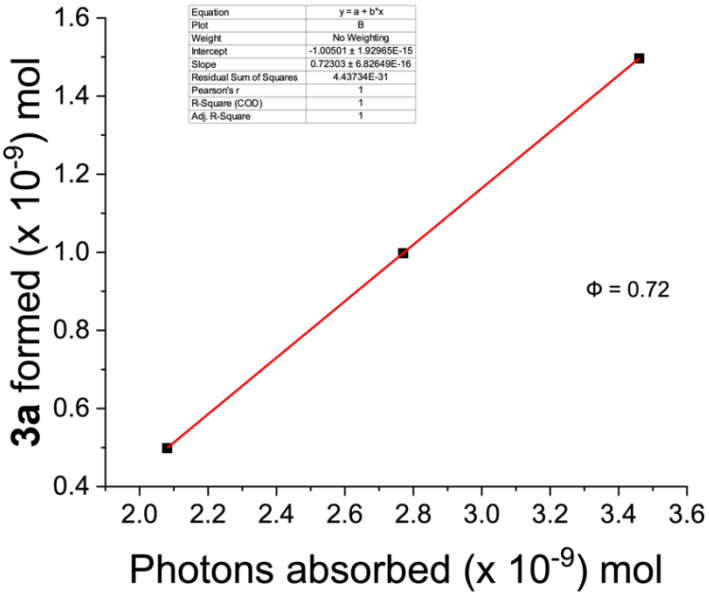

Figure 46. Graph showing the amount of **3a** formed under different light intensity (0.7–2.0 mW/cm^2). Photons absorbed by **3** were calculated and the slope of the graph gives the quantum yield for the photocleavage reaction

ε_1	Φ
9020	0.72

Table 3. Table showing the calculated values and photocleavage reaction quantum yield of **3** at 405 nm light irradiation.

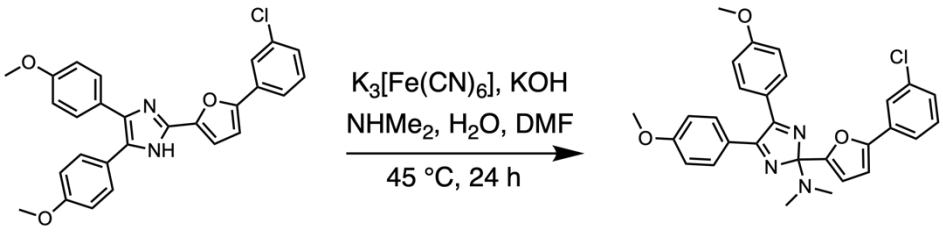

Scheme 6. Synthetic scheme for **4**.

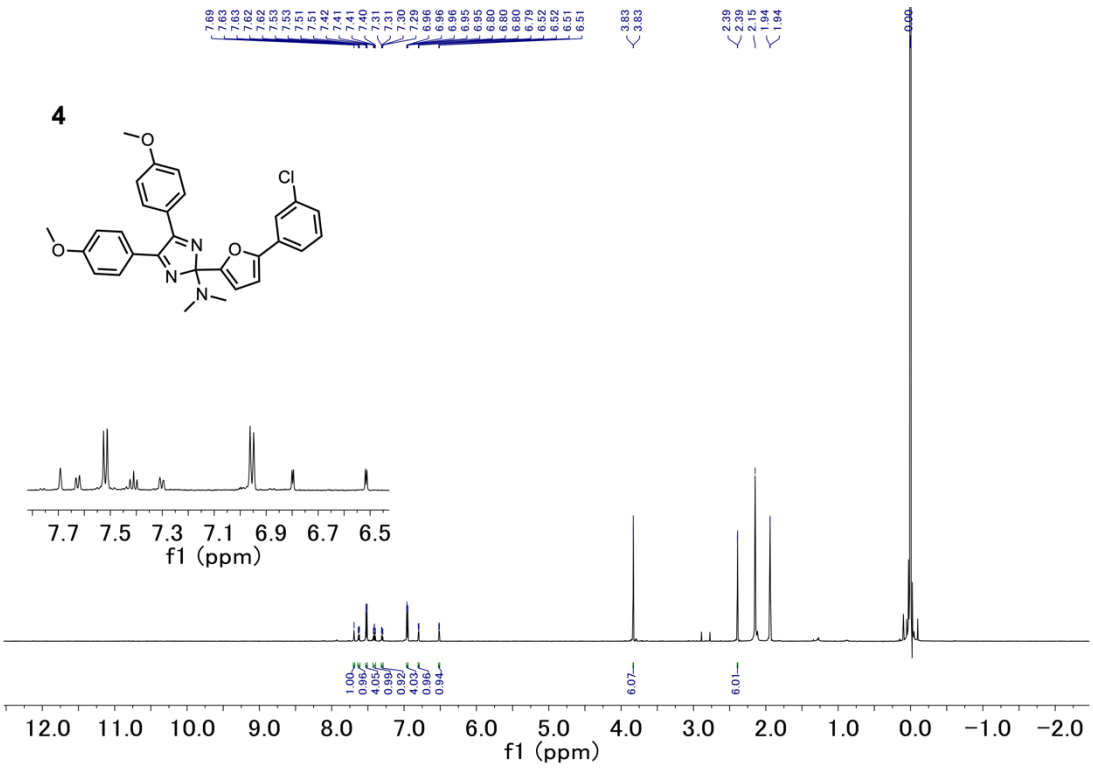

Figure 47. ^{1}H NMR spectrum of **4** recorded in acetonitrile-d_3.

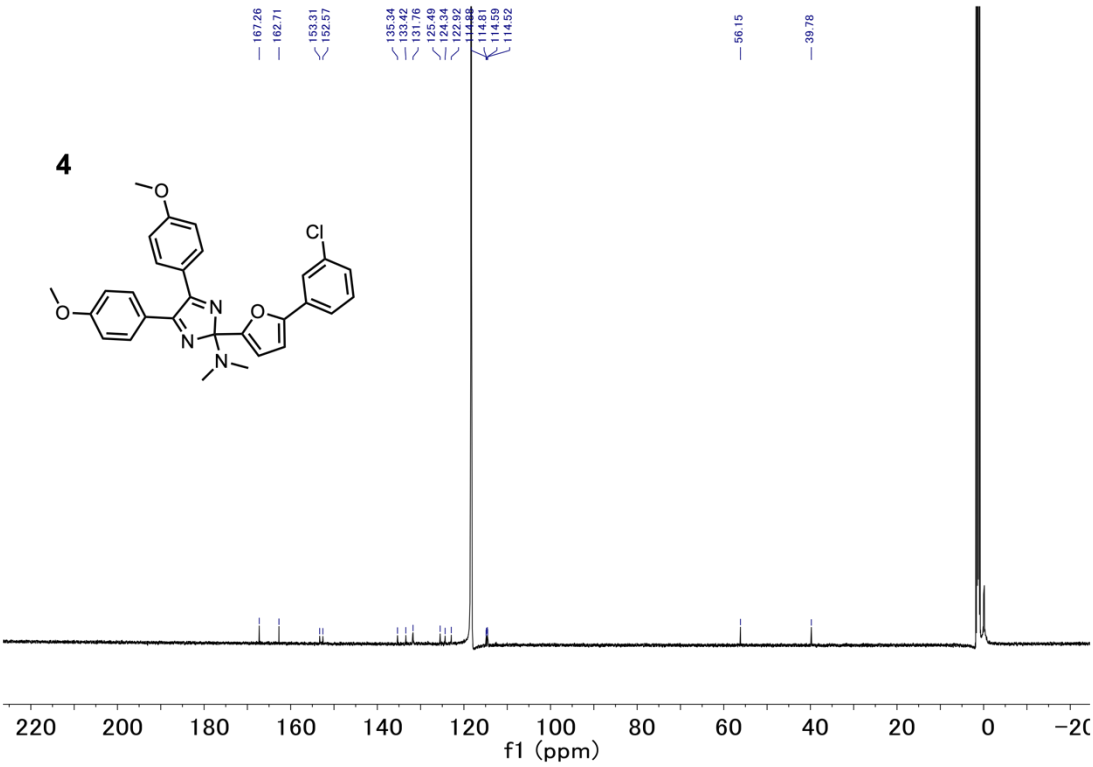

Figure 48. ^{13}C NMR spectrum of **4** recorded in acetonitrile-d_3.

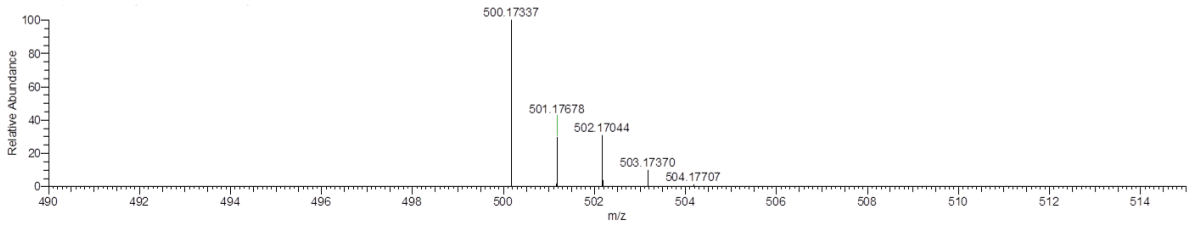

Figure 49. High resolution mass spectra (ESI) of **4** - m/z $[M+H]^+$ calculated for $C_{29}H_{26}ClN_3O_3$: 500.17409, found: 500.17337.

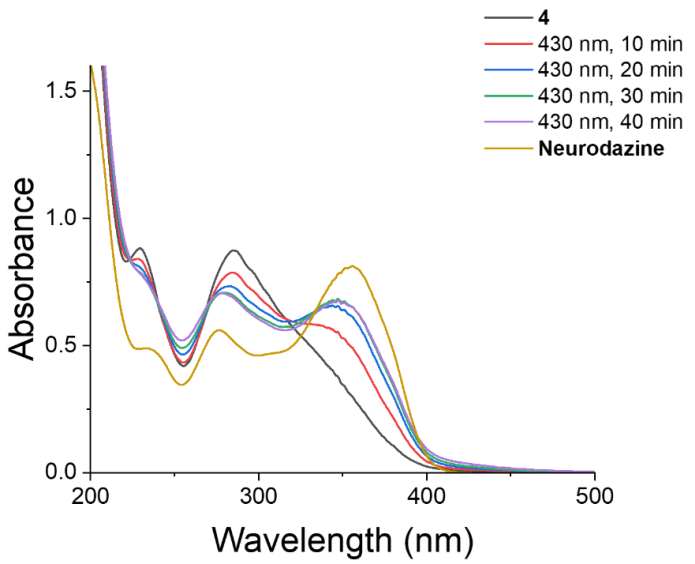

Figure 50. UV-visible absorption spectra of **4** recorded in acetonitrile:water (1:1) mixture upon irradiating with 430 nm light for different time periods and UV-visible absorption spectrum of **Neurodazine**.

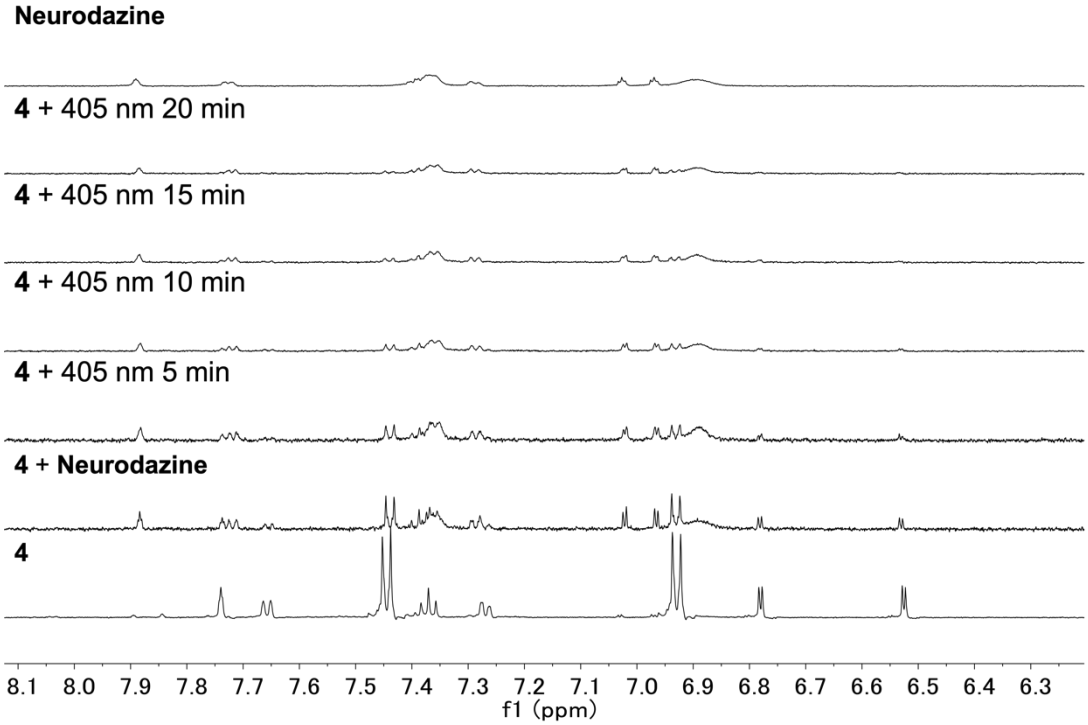

Figure S51. ^{1}H NMR spectra of **Neurodazine** (top), **4** (bottom), and **4** containing Neurodazine as an internal reference in 3:4 molar ratio after irradiated with 405 nm light for 20 minutes (middle) recorded in acetonitrile-d_3 and D_2O (1:1) mixture degassed using argon for 1 h.

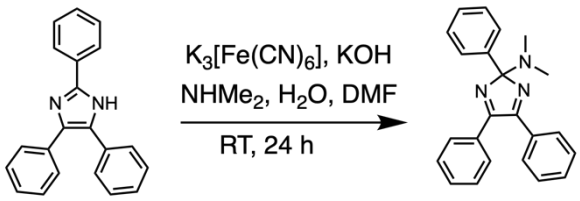

Scheme 7. Synthetic scheme for **5**.

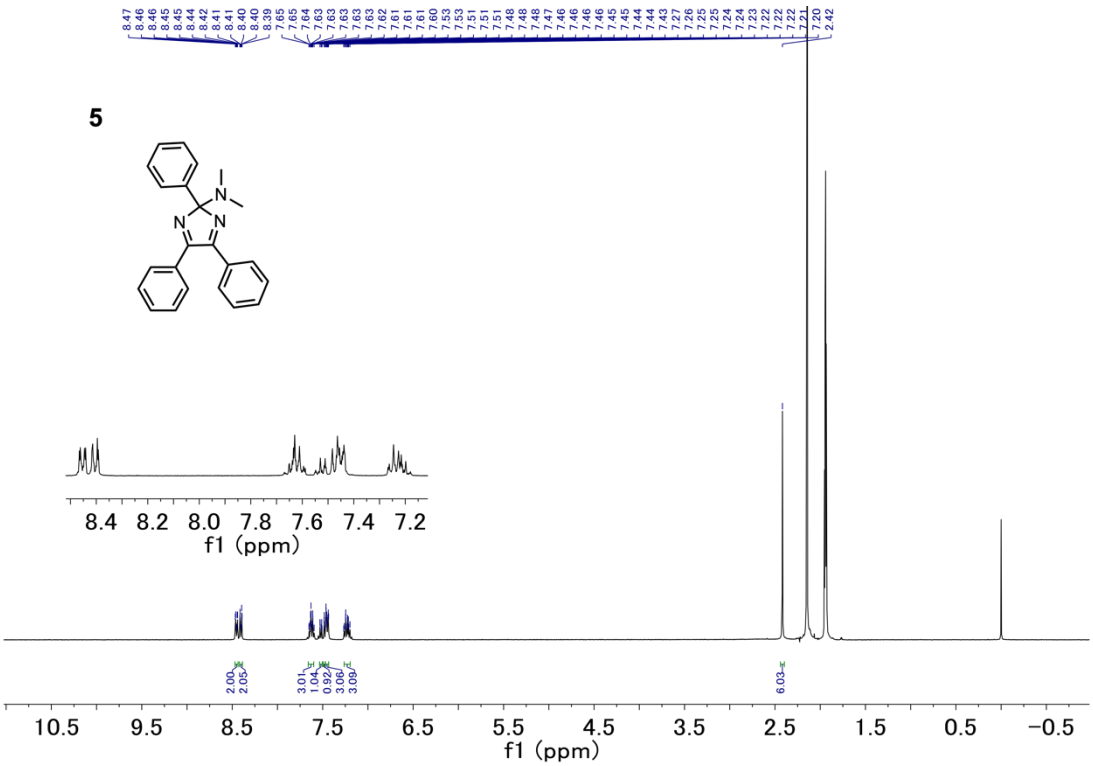

Figure 52. ^{1}H NMR spectrum of **5** recorded in acetonitrile-d_3.

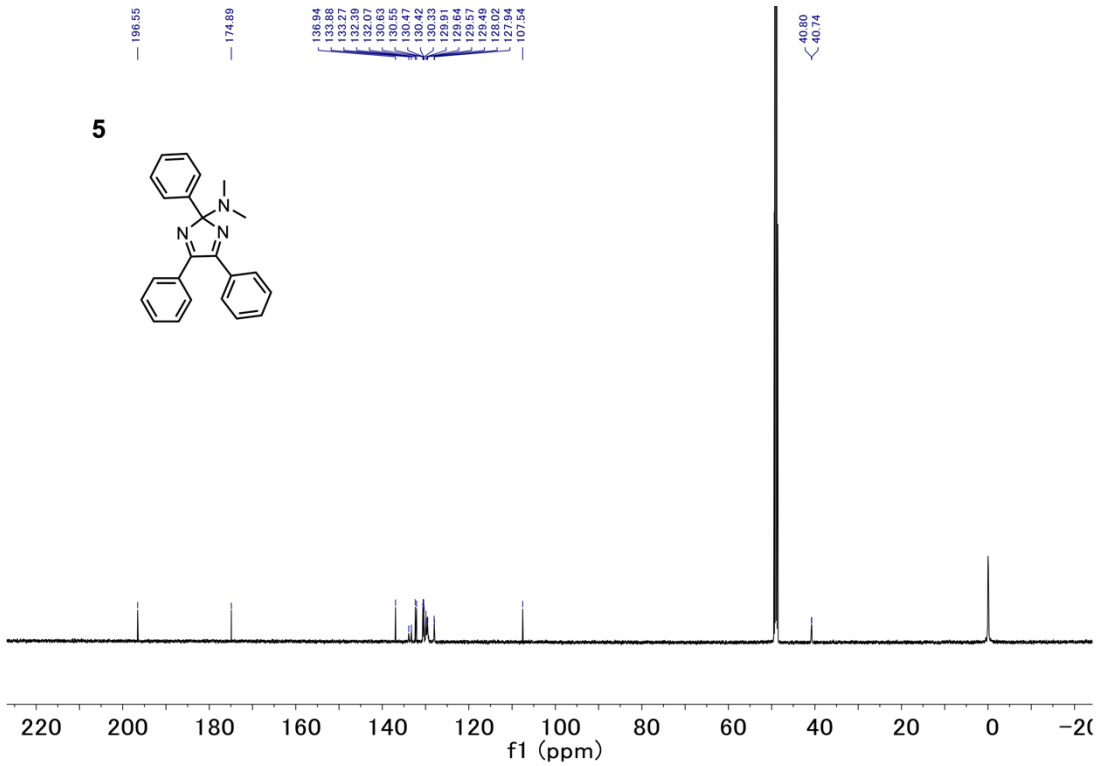

Figure 53. ^{13}C NMR spectrum of **5** recorded in CD_3OD.

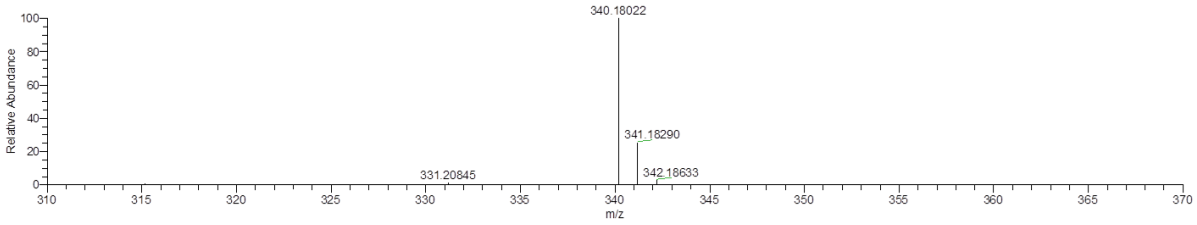

Figure 54. High resolution mass spectra (ESI) of **5** - m/z $[M+H]^+$ calculated for $C_{23}H_{21}N_3$: 340.18137, found: 340.18022.

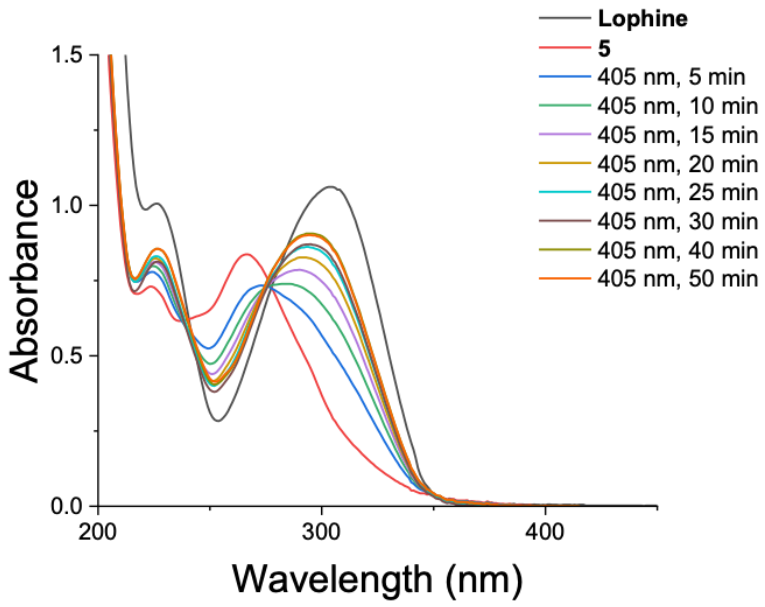

Figure 55. UV-visible absorption spectra of **5** recorded in acetonitrile:water (9:1) mixture upon irradiating with 405 nm light for different time periods and UV-visible absorption spectrum of **Lophine**.

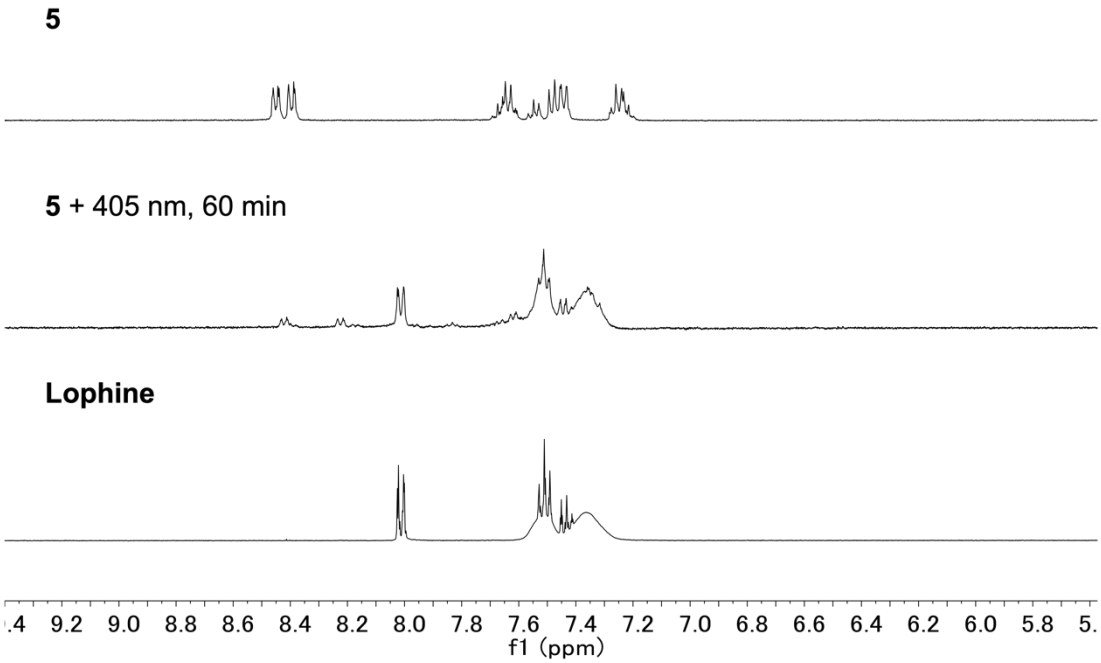

Figure 56. ^{1}H NMR spectra of **Lophine**, **5**, and **5** after irradiated with 405 nm light for 60 minutes recorded in acetonitrile-d_3 and D_2O (9:1) mixture.

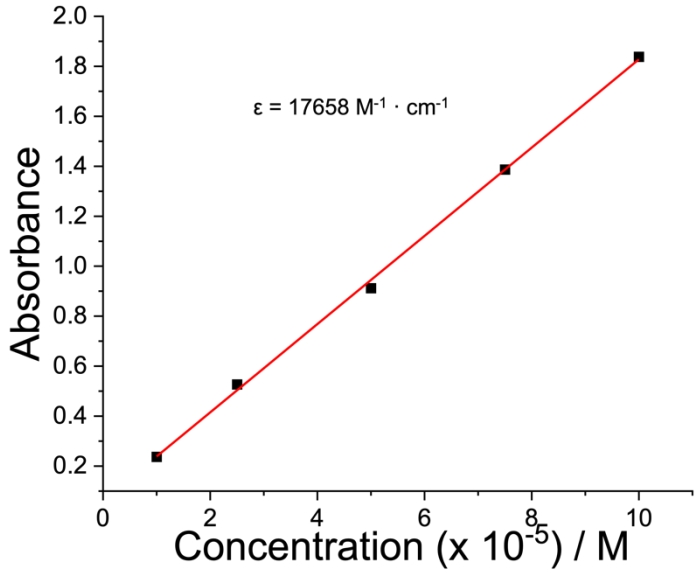

Figure 57. Graph of varying concentration of **5** against absorbance at λ_{max} (266 nm, red line). Extinction coefficient of **2** was calculated from the slope of a linear fit.

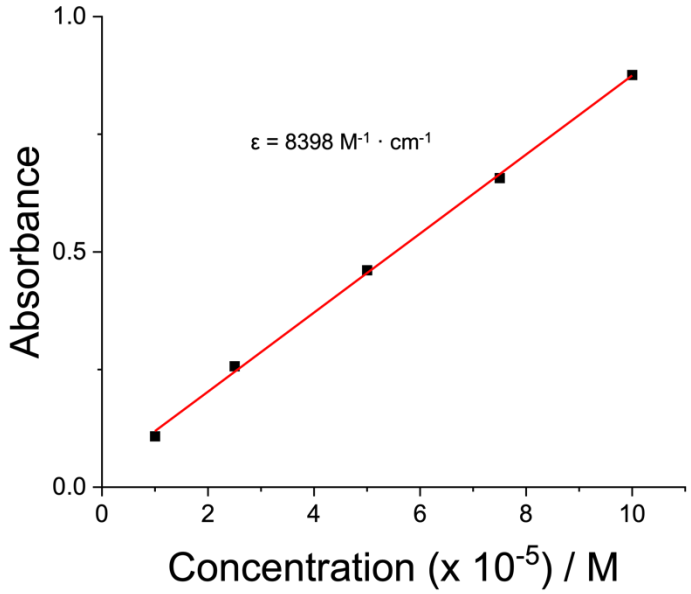

Figure 58. Graph of varying concentration of **Lophine** against absorbance at λ_{max} (266 nm, red line). Extinction coefficient of **Lophine** was calculated from the slope of a linear fit.

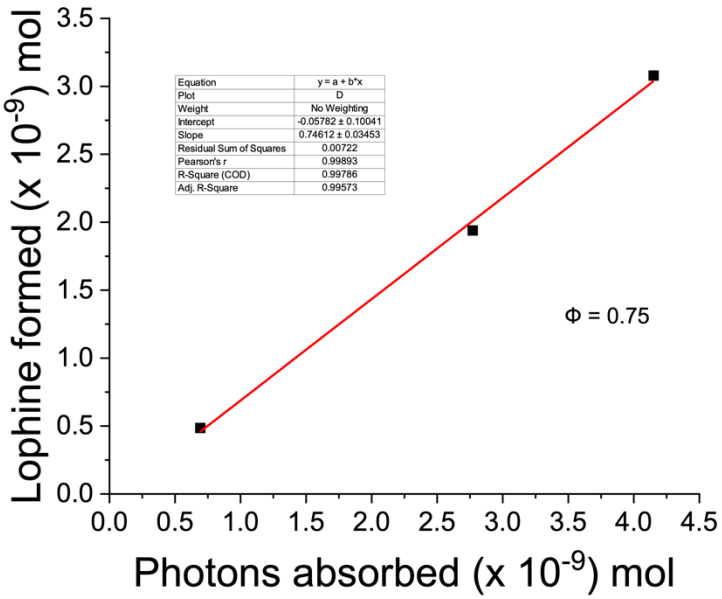

Figure 59. Graph showing the amount of **Lophine** formed under different light intensity (0.7–2.0 mW/cm^2). Photons absorbed by **5** were calculated and the slope of the graph gives the quantum yield for the photocleavage reaction of **5**.

ε_1	$\varepsilon_{Lophine}$	Φ
17658	8398	0.75

Table 4. Table showing the calculated values and photocleavage reaction quantum yield of **5** at 405 nm light irradiation.

3. Discussion

To efficiently enable light-induced modulation of biological functionality, a photosensitive pharmaceutical agent must meet specific criteria, including a significantly altered molecular structure, transition from a photocaged to uncaged form, and a substantial difference in activity levels between these two configurations. Ideally, photocleavage should be accomplished using light with the ability to considerably penetrate tissues with minimal cellular detriment, such as that achieved with longer visible wavelengths. With these considerations in mind, I embarked on developing a new caging method with triarylimidazoles as the primary target. Caging the triarylimidazole moiety would have the potential to convert a broad family of triarylimidazole-based drug molecules into photoactivatable drugs.

The photochromic attributes of the hexaarylbiimidazole (HABI) molecule have undergone extensive investigation.[31] When exposed to UV light irradiation, the covalent C–N bond connecting the two imidazole rings undergoes homolytic cleavage, producing a pair of colored 2,4,5-triphenylimidazolyl radicals. These radicals regenerate HABI

in inert solvent, such as benzene, or form 2,4,5-triphenylimidazole in the presence of a hydrogen donor.

Our initial attempts to dimerize SB431542 using standard oxidative conditions in a biphasic system of benzene and water failed due to the extremely low solubility of SB431542 in benzene. Subsequently, I obtained the dimethylamino adduct of SB431542 rather than the desired dimer when I substituted DMF as the solvent instead of benzene due to a reaction between the SB431542 radical and trace amounts of dimethylamine present as impurities in DMF. Only one prior report32 mentioned the diethylamino adduct of phenanthroimidazole, a molecule related to our newly synthesized molecules. However, the previous study primarily focused on the photochemical reaction of the diethylamino adduct to the phenanthroimidazole dimer in inert benzene solvent. In our case, irradiation of 1 and 2 with 405 nm light in the aqueous medium regenerated the original SB431542 molecule. I propose that the C–N bond connecting the carbon atom of the imidazole ring in SB431542 and the nitrogen atom of the dimethylamino group undergoes homolytic cleavage upon

exposure to 405 nm light irradiation, generating imidazolyl and dimethylamino free radicals. The formation of free radicals, which indicates a free radical mechanism, was qualitatively confirmed by observing photo-induced electron spin resonance during the spin trapping experiment with **5** (Figure 60). The imidazolyl radical likely accepts a hydrogen atom from the dimethylamino radical in the photochemical cage or the aqueous medium, leading to reformation of the original SB431542 molecule. The dimethylamino free radical can form the formylidene methylamine (CH2=NCH3) by releasing a hydrogen atom. Subsequently, it undergoes hydrolysis to yield the methylamine and formaldehyde, as depicted in the reaction scheme (Figure 61)[33]. In each photoreaction mixture involving compounds **1**, **3**, or **5**, I observed proton peaks at approximately 4.7 ppm and 2.3 ppm, assignable to protons for formaldehyde and methylamine, respectively (Figure 62- 64).

The formation of **SB431542** from **1** or **2** upon irradiation with visible light (405 nm) was confirmed via UV-visible absorption spectroscopy, ^{1}H NMR, and HPLC analyses (Figure 8, 12, 14 and Scheme 4). Fortunately, our photochemical reaction showed high efficiency, as approximately 96% of **SB431542** was recovered from **1** according to HPLC analysis (Figure 1d), highlighting the efficiency of our photochemical reaction.

In our molecular design, although the dimethylamino and N-methyl-(N-hydroxycarbonylmethyl) amino groups introduced as photoremovable groups are small, their introduction on the imidazole ring's carbon atom could induce a significant change in the molecule's binding affinity to the target kinases. This was due to the hybridization state of the carbon atom of the imidazole ring changing from sp^2 to sp^3, which inherently altered the molecular core structure from planar imidazole to tetrahedral 2*H*-imidazole. The molecular docking simulation results supported these suppositions, showing lower binding affinities for **1** and **2** than for **SB431542** (Figure 36).

The immunoblotting experiment revealed that both **SB431542** and compound **1** exhibit differences in their inhibitory activity by affecting the activation of Smad2. This activation is dependent on the phosphorylation process mediated by TGF-β R1 (Figure 24a and b). These findings provide clear molecular evidence that **1** regulates TGF-β-mediated phosphorylation of Smad2 in a photoresponsive manner.

Further, the wound healing assays with MDA-MB-231 cells confirmed the suppositions and validated our caging strategy. Cells treated with TGF-β1 and **SB431542** exhibited wound recovery almost identical to that in the control experiment (Figure 28a(iv)), indicating the inhibitory effect of **SB431542**. Conversely, treating cells with TGF-β1 and **1** resulted in similar wound recovery as exhibited by those treated solely with TGF-β1, indicating the non-inhibitory effect of **1** towards TGF-β R1 (Figure 28a(v)). Irradiating cells treated with TGF-β1 and **1** with 405 nm light for 3 min inhibited the TGF-β R1–mediated wound healing process, confirming that **1** underwent photocleavage to produce **SB431542** (Figure 28a(vi)).

The results of the spatiotemporal regulation experiment demonstrated the applicability of our strategy for achieving external regulation of drug activity to minimize the adverse effects associated with cancer therapy (Figure 31). The wound at the light-irradiated area exhibited minimal wound recovery (gap reduction of approximately 27 μm), resulting from photocleavage of **1** leading to formation of **SB431542** and subsequent inhibition of the TGF-β R1–mediated wound recovery process. In contrast, the wound covered by aluminum foil displayed greater wound recovery (gap reduction of approximately 69 μm), which was attributed to the non-inhibitory nature of **1**. The results of this experiment clearly demonstrated the ability of these molecules to aid site-selective drug activity upon light irradiation.

Oxidizing another imidazole-based drug molecule, **adezmapimod**, with dimethylamine under strong basic conditions led to replacement of the fluorine atom on the phenyl ring with the dimethylamino group, along with introduction of the dimethylamino group on the carbon atom of the imidazole ring (Figure 38b). Despite this sensitivity to the strong basic conditions, the molecule underwent successful photochemical cleavage upon visible light irradiation (Figures 38a, b, and 39).

The successful caging and uncaging reactions observed for neurodazine and 2,4,5-triphenylimidazole, in contrast to the unsuccessful caging of 2,5-diphenyl-1H-imidazole, 2-phenylbenzimidazole, and 2-phenylimidazole, highlight the importance of imidazole-based molecules with aromatic ring substitutions at positions 2, 4, and 5. These substituted

imidazoles are ideal candidates for adding the dimethylamino group on the carbon atom of the imidazole ring. The trend can be attributed to the additional stabilization effect provided by the aromatic rings, which aids in delocalizing the free radical within the molecule generated under ferrocyanide oxidation conditions. However, the free radicals generated in the case of 2,5-diphenyl-1*H*-imidazole, 2-phenylbenzimidazole, and 2-phenylimidazole lack sufficient stabilization through delocalization, rendering them unable to react with dimethylamine.

Utilizing blue light in the 400-450 nm range for uncaging within our system offers a significant advantage, as visible light inflicts less harm on living cells compared to UV light. However, this benefit is tempered by the fact that shorter-wavelength visible light struggles to penetrate blood-supported tissue efficiently, owing to the absorption by biomolecules such as hemoglobin. Nonetheless, I am confident that recent engineering and materials advancements are addressing these penetration challenges. For instance, the implementation of wireless subdermal electronics[34a-b] or multi-modal fiber optics technology[11c] or light conversion materials[35] allows us to position the irradiation source directly adjacent to the targeted site. This strategic placement effectively bypasses the limitations of deep light penetration, ensuring precise and localized treatment.

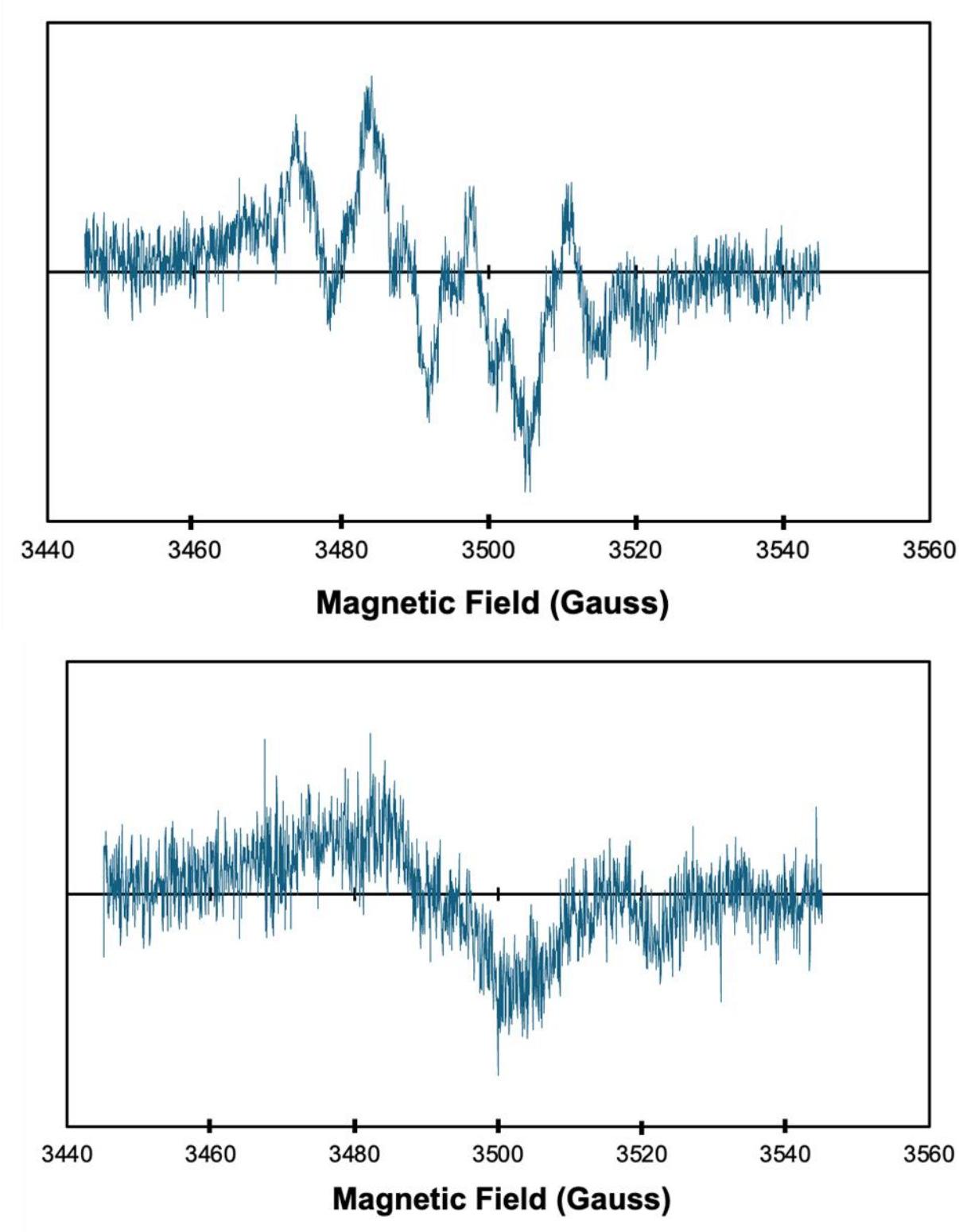

Figure 60. (a) ESR spectrum of **5** in the presence of DMPO after irradiation. (b) ESR spectrum of **5** in the presence of DMPO before irradiation. A distinct ESR signal with fine-structure splitting was observed only after irradiation, which indicates the radical formation during the photoreaction of **5**.

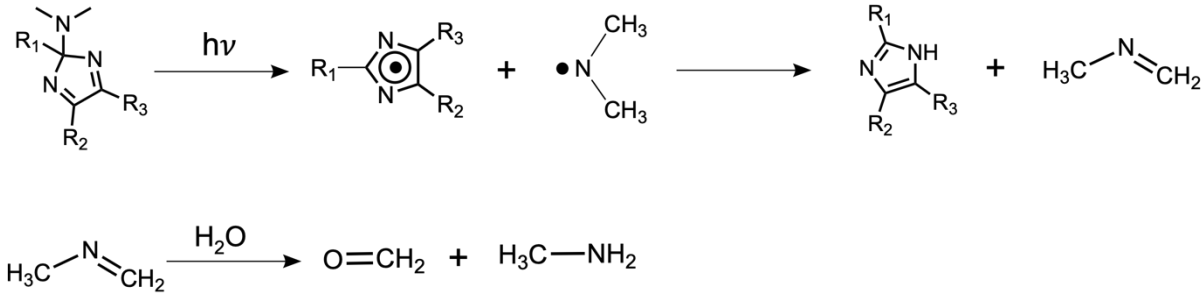

Figure 61. Scheme presenting the homolytic cleavage of C-N bond linking the imidazole ring and dimethylamine group by light and fate of the dimethylamine radical post photochemical reaction.

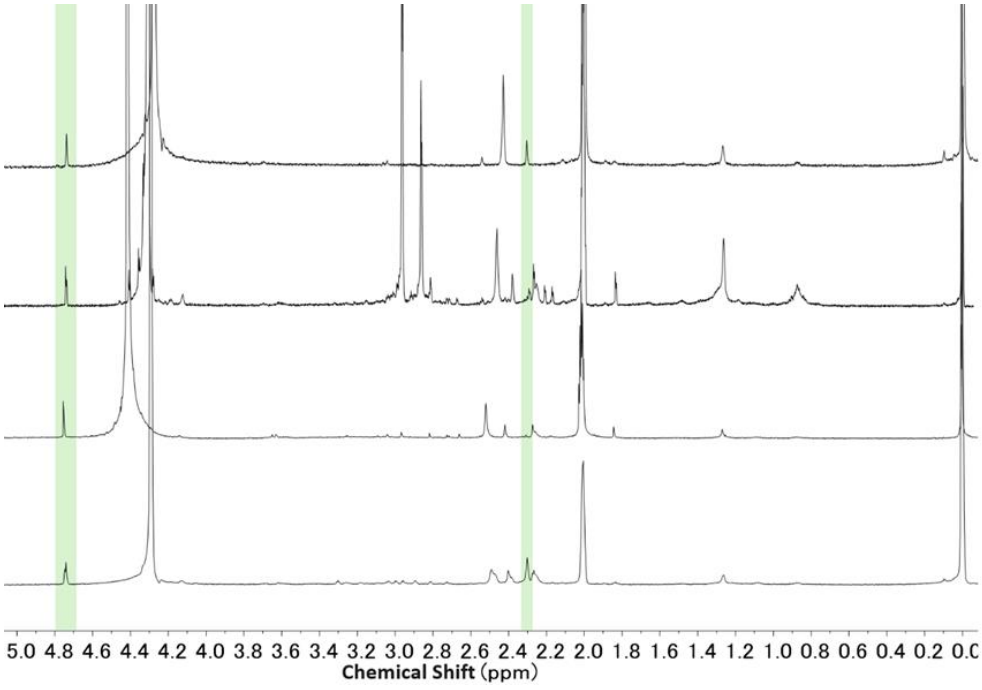

Figure 62. ^{1}H NMR spectra obtained after the photochemical cleavage of compounds (a) **5**, (b) **3**, (c) **2** and (d) **1** in acetonitrile-d_3 and D_2O (1:1) mixture confirming the peaks at around 4.7 ppm and 2.3 ppm for the proton of formaldehyde and methylamine in the solution of **5**, **3** and **1**, respectively.

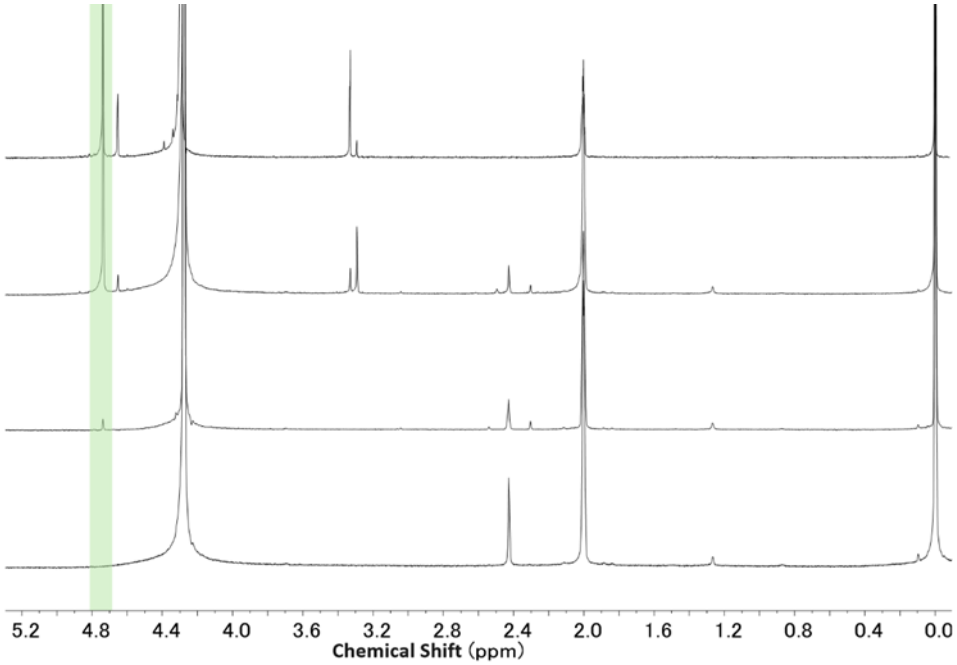

Figure 63. ^{1}H NMR Spectral Analysis of Photoreaction Products (a) **5** in acetonitrile-d_3 and D_2O (1:1) mixture before irradiation; no significant peak at 4.7 ppm. (b) **5** in acetonitrile-d_3 and D_2O (1:1) mixture after irradiation; emergence of a peak at approximately 4.7 ppm. (c) The solution from (b) after the addition of formaldehyde; the 4.7 ppm peak is enhanced. (d) Formaldehyde in acetonitrile-d_3 and D_2O (1:1) mixture; a distinct peak at 4.7 ppm corresponding to formaldehyde, which overlaps with the photochemically generated peak from **5**. The observed NMR peaks at 4.65, 3.30, and 3.29 ppm are attributed to impurities in the formaldehyde sample.

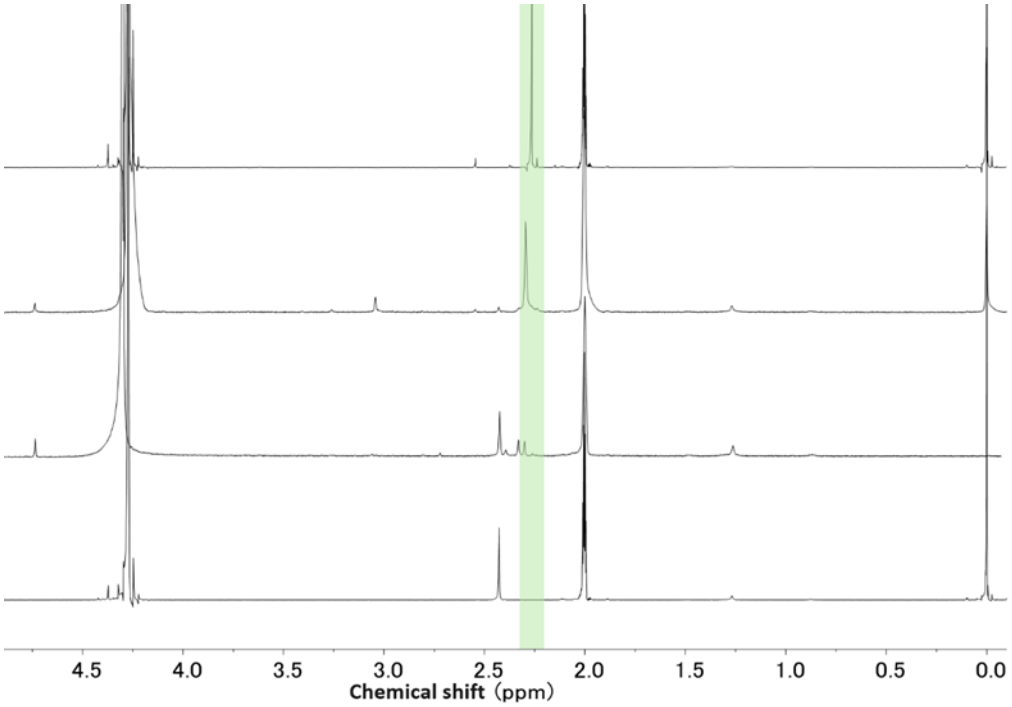

Figure 66. ^{1}H NMR Spectral Analysis of Photoreaction Products (a) **5** in acetonitrile-d_3 and D_2O (1:1) mixture before irradiation; no significant peak at 2.3 ppm. (b) **5** in acetonitrile-d_3 and D_2O (1:1) mixture after irradiation; emergence of a peak at approximately 2.3 ppm. (c) The solution from (b) after the addition of methylamine; the 2.3 ppm peak enhanced. (d) Methylamine in acetonitrile-d_3 and D_2O (1:1) mixture; a distinct peak at 2.3 ppm

4. Conclusion

I developed a new caging method to transform triarylimidazole-based drug molecules into visible light– activatable drugs. The photoresponsive versions of **SB431542** generated through the incorporation of a photocleavable C–N bond could be precisely activated using visible light irradiation, affording meticulous control over drug activity. Spatiotemporal wound healing assays conducted with human breast cancer cells highlighted the method's potential to selectively target cancer cells within specific regions, leaving normal cells unharmed. Beyond its applications in therapeutic applications, our strategy also holds significant promise as a versatile research tool, facilitating the study of specific molecules and pathways within cells by enabling the activation or inhibition of target proteins, which will help to elucidate their roles in biological processes. I am currently conducting research to expand the applicability of the present method of photocaging bioactive compounds by introducing a dialkylamino group, which I proposed this time, to compounds other than imidazole derivatives.

5. Experimental Section

5.1 Chemicals

The biochemical agents, cell culture medium, and a variety of chemicals were procured from commercial vendors, including Fujifilm Wako Pure Chemical Corporation, Tokyo Chemical Industry Co., Ltd., Merck, Kanto Chemicals, and BLD pharmatech Ltd. These materials were employed in their original condition without any further purification.

5.2 Instruments

Reactions were monitored through thin-layer chromatography (TLC) using TLC silica gel 60 RP-18 $F_{254}S$ and TLC silica gel 60 F_{254} (Merck) plates.

The compounds were purified by silica gel column chromatography and by preparative HPLC. I employed silica gel 60 N (spherical, neutral, 63-210 μm, Kanto chemicals) for column purification. For preparative HPLC I used Shimadzu high performance liquid chromatography (UV/Vis detector: SPD-20A; fraction collector: FRC-10A; degassing unit: DGU-20A; communications bus module: CBM-20A; liquid chromatograph: LC-20AT) with a preparative column (TOSOH, 0DS-80T) and an analytical column (COSMOSIL, 38020-41).

NMR spectra (^{1}H, ^{13}C) were recorded using a JEOL ECX-400 (400 MHz) and JEOL ECX-600 (600 MHz) spectrometer. Molecular weights were determined by electrospray ionization mass spectrometry (ESI-MS) using Exactive™ Plus Hybrid Quadrupole/Orbitrap mass spectrometer.

UV-visible absorption spectra were measured using a Shimadzu UV spectrophotometer (UV1800) equipped with a TCC-100 Shimadzu temperature-controlled cell holder. Photocleavage reactions of the synthesized compounds were carried out using an LED light source (Asahi Spectra, CL-1503) with 405 nm, 430 nm, and 450 nm LED heads. The light intensity was measured by broadband power/energy meter (MELLES GRIOT 13PEM001).

The cells used in this study were cultured using the PHCbi MCO-175-PJ incubator by Panasonic, the Panasonic MCO-170AIC incubator, and the AS ONE E-22 CO_2 incubator. The human breast cancer cells (MDA-MB-231) used in wound healing assay were cultured and maintained at 37 ℃ in a humidified incubator in the presence of 5% CO_2.

Photographs were captured using two different microscopy setups. The Nikon Eclipse Ts2 microscope and the OLYMPUS BX60 microscope were utilized, both were equipped with an Moticam 1080 digital camera.

Centrifugation procedures were performed using the TOMY LC-220 centrifuge and the KUBOTA 3220 centrifuge.

5.3 Wound Healing Assay

I washed MDA-MD-231 cells by D-PBS (-) (Wako) and subjected them to a treatment involving 0.25% trypsin (Wako, 0.25%w/v trypsin-1 mmol/L EDTA·4Na solution with phenol red), followed by incubation at 37 ºC for 5 minutes to facilitate their detachment from the culture dish. Subsequently, the detached cells were resuspended in DMEM (Wako, high glucose with L-Glutamine, phenol red and sodium pyruvate) medium to neutralize the trypsin activity and used for wound healing assay.

New medium was then added to achieve MDA-MB-231 cells at the concentration of 2 x 10^5/ml, and samples corresponding to either 24-well or 6-well plates were prepared accordingly.

I determined the EC_{50} values of **SB431542**, **1**, and **2** by performing the wound healing assay at different concentrations.

The cells were allowed to adhere for a duration about 2 days until the confluence is close to 100%. Subsequently, a serum-starvation phase of 32 hours was imposed prior to the initiation of the cell wound. The introduction of wounding across the cellular monolayer was achieved by creating a cell-free zone through scratching with a pipette tip. The inflicted cellular wound sites were then subjected to different treatment conditions. In the control experiment, only DMSO (0.13% v/v) was added to the medium. In all other cases, such as TGF-β1 (3 ng/mL) **SB431542** (10 μM), **1** (10 μM), and **2** (10 μM), they were dissolved in

DMSO (0.13% v/v) and then added to the medium and incubated for a period of 24 hours at 37 °C in a humidified incubator in the presence of 5% CO_2. The migration of cells into wound area was observed and recorded using a microscope. To check the effect of 405 nm light irradiation on wound healing process resulting from the photocleavage reactions of **1** and **2** producing **SB431542**, I irradiated the sample wells for 3 minutes with the 405 nm light at a 15.5 mW/cm^2 intensity. For spatiotemporal regulation experiment I irradiated the cells with 405 nm light for 24 hours at a 0.1 mW/cm^2 intensity.

Finally, the acquired microscopic images were analyzed using ImageJ, an image analysis software. The wound gap width was tracked by drawing lines along the leading edges of each cell front, and the average wound recovery was calculated, as described below.

5.4 Calculation of Average Wound Recovery

The average wound recovery (WR) was calculated according to the following formula,

$$WR = (A_1-A_2)/2L$$

WR: Average wound recovery

A_1: Total area of the wound at time t = 0 h

A_2: Total area of the wound at time t = 24 h

L: Length of the selected wound area

5.5 Immunoblotting Experiment

Cell culture: The human breast cancer cell line MDA-MB-231 (ATCC; HTB-26) and human glioblastoma cell line KMG4 (International Cell Line Authentication Committee (ICLAC) accession number CVCL_JZ69) were cultured in Dulbecco's modified Eagle's medium (DMEM) containing 10% fetal bovine serum (FBS). Both cells were cultured at 37 °C under a humidified atmosphere containing 5% CO_2.

Treatment with 1: The MDA-MB-231 and KMG4 cells were serum starved for 14

hours in FBS-depleted DMEM, and then treated with 10 μM **SB431542** or 10 μM **1** for 15 min. Cells were exposed to 405 nm light for 10 min, incubated for 5 min, followed by stimulation with 10 ng/ml TGF-β. After 30 min, the cells were lysed with RIPA buffer for immunoblotting.

Immunoblotting: Cells were lysed with lysis buffer [10 mM Tris-HCl (pH 7.4), 5 mM EDTA, 150 mM NaCl, 10% glycerol, 1% Triton X-100, 1% sodium deoxycholate, 0.1% SDS, 50 mM NaF, 1 mM phenylmethylsulfonyl fluoride (PMSF), and 1 mM sodium orthovanadate (Na_3VO_4)] and a protease inhibitor mixture [Complete (EDTA-free) protease inhibitor (Roche, Basel, Switzerland)] for 20 min on ice and centrifuged at 15,000 rpm for 10 min at 4°C. Supernatants were subjected to SDS- PAGE, and separated proteins were transferred to a polyvinylidene difluoride membrane (Millipore, Billerica, MA). The membranes were incubated with primary antibodies at 4°C overnight, followed by treatment with horseradish peroxidase-labelled secondary antibodies. The signals were developed using ECL™ Western Blotting Detection Reagents (GE Healthcare, Little Chalfont, UK) and visualized with a LAS 4000 mini (GE Healthcare). Antibodies used in this experiment are as follows: anti-phospho-Smad2 (S465/467), anti-Smad2 (Cell Signaling Technologies), anti-Actin (clone C4) (Millipore).

5.6 Molecular Docking

The structure of TGF-β R1 (PDB:3TZM) was used for docking, wherein the binding site of **SB431542** (4-[5-(1,3-benzodioxol-5-yl)-4-(pyridin-2-yl)-1*H*-imidazol-2-yl]benzamide) was used as the docking site. 3D models of three ligands (**SB431542**, **1**, and **2**) were generated based on their SMILES strings. Autodock tools were used to prepare receptor and ligands, where only polar hydrogens were included, and the ligands rotatable angles were defined. Finally, a grid box with the dimension of (46, 40, 46) with spacing of 0.375 Å centered around the ligand binding site in the PDB structure (x = 4.152 Å, y = 8.837 Å, z = 8.328 Å) was set up. All ligands including **SB431542** were docked using the

same grid. The top 10 poses from each simulation were retained and analyzed. All docking simulations were performed using Autodock Vina (1.1.2).[36]

5.7 Equipments Used for Quantum Yield Measurement:

LED light source: Asahi Spectra, CL-1503 equipped with 405 nm LED head.

Lens: Olympus microscope condenser U-POC-2.

5.8 Calibration Curves and Photochemical Conversion Efficiency

Using the calibration curves obtained by plotting the different concentrations of the molecule against the corresponding areas under the HPLC peaks, I tried to estimate the yield of SB431542 formed by the photocleavage of 1. Our observations revealed that subjecting the solution of 1, initially possessing a concentration of 6.14×10^{-5} M, to irradiation with 405 nm light for a duration of 10 minutes yielded a resultant concentration of 5.88×10^{-5} M of SB431542. This outcome suggests a conversion of approximately 96%. Similarly, UV-visible absorption spectrum of compound 2 having the concentration of 3.61×10^{-5} M upon 405 nm light irradiation produced 3.49×10^{-5} M of SB431542 indicating the conversion efficiency of approximately 97%.

5.9 Quantum Yield Calculation

The quantum yield for the photoreaction of compound **1** to form **SB431542** was assessed in the following manner.

$$\Phi_{\mathbf{1}-SB431542} = \frac{\text{number of events}}{\text{number of photons absorbed}} = \frac{\text{number of } \mathbf{SB431542} \text{ formed (mol)}}{\text{number of photons absorbed (mol)}}$$

a. Determination of **SB431542** molecules formed

The photocleavage reaction conversion ratios were strictly kept minimum (< 4%) during the experiments to reduce the photons absorbed by **1**. The calculation of the number of **SB431542** molecules generated was carried out using the following equation:

$$\text{Number of } \mathbf{SB431542} \text{ formed} = \frac{A_{BI} - A_{AI}}{(\varepsilon_{\mathbf{1}} - \varepsilon_{\boldsymbol{SB431542}})l} V$$

A_{BI} Absorbance at λ = 262 nm before irradiation

A_{AI} Absorbance at λ = 262 nm after irradiation

$\varepsilon_{\boldsymbol{1}}$ Extinction coefficient of **1** at λ_{max} = 262 nm

$\varepsilon_{\boldsymbol{SB431542}}$ Extinction coefficient of **SB431542** at λ = 262 nm

l Optical length of cuvette (*i.e.,* 1 cm)

V Total volume of the sample solution

b. Determination of absorbed photons

Actinometry was employed using a ferrioxalate actinometer to measure the absorbed photons.[37] I established our experimental arrangement in accordance with previously documented procedures.[38] A round cuvette containing the ferrioxalate actinometer solution (with a total volume of 3.1 mL and an optical path length of 1 cm) was positioned in front of a square cuvette (with an optical path length of 1 cm) that featured a magnetic stirring bar to capture all photons passing through it. Both cuvettes were affixed to a metal base to ensure consistent positioning throughout all experiments.

c. Procedure for the measurement

The procedure has following steps.

(1) Determination of absorbed photons by the blank solution:

This is done by exposing the cuvettes containing a blank solution (consisting of CH_3CN and water in a 1:1 ratio, totaling 1.5 mL) and a ferrioxalate actinometer solution (0.15 M, 3 mL) to 405 nm light (with an intensity ranging from 0.15 to 0.56 W/cm^2) for 60 seconds. Subsequently, the actinometer solution was manually shaken, and 1 mL of it was transferred to a glass vial. This portion was then mixed with sodium acetate buffer (0.15 M, 2 mL) containing phenanthroline (0.1 wt%, 300 μL). The resulting mixture was incubated for

approximately 60 minutes, after which its absorbance was measured at 510 nm using absorption spectroscopy.

(2) Determination of absorbed photons by the sample solution of **1**:

Stock solution of **1** (75 µL, 1 mM) was added to the same square cuvette containing the CH_3CN and water (1:1) solvent (1.425 mL) to create the sample solution of **1** (1.5 mL, 50 µM). A fresh ferrioxalate actinometer solution (0.15 M, 3 mL) was introduced into the round cuvette, followed by light irradiation (405 nm, 0.15–0.56 mW/cm^2, 60 sec). The actinometer solution was then manually shaken, and 1 mL of it was transferred to a glass vial. To this portion, sodium acetate buffer (0.15 M, 2 mL) containing phenanthroline (0.1 wt%, 300 µL) was added, and the mixture was incubated for approximately 60 minutes. Finally, absorbance at 510 nm was measured using absorption spectroscopy. All experiments were conducted in a dark room, with the use of red light when necessary. The number of absorbed photons was calculated using the provided equation:

$$\text{Photons absorbed} = \frac{(A_0 - A_1)V_1V_3}{\varepsilon_{510\,nm}V_2\phi_{405\,nm}}$$

A_0 Absorbance of ferrioxalate-phenanthroline solution at 510 nm (with pure solvent in the square-shaped cuvette)

A_1 Absorbance of ferrioxalate-phenanthroline solution at 510 nm (with solution of **1** in the square-shaped cuvette)

V_1 Volume of actinometer solution in round-shaped cuvette (*i.e.,* 3 mL)

V_2 Volume of actinometer solution taken from round-shaped cuvette after irradiation (*i.e.,* 1 mL)

V_3 Total volume of the ferrioxalate-phenanthroline solution (*i.e.,* 3 mL).

$\mathcal{E}_{510nm}$ Extinction coefficient of ferrioxalate-phenanthroline complex (ferroin) at 510 nm (obtained by calibration graph, ε = 11410 $M^{-1}\cdot cm^{-1}$ in our experimental condition) (Figure 65)

ϕ_{405nm} Quantum yield of ferrioxalate actinometer at irradiation wavelength (1.14 at 405 nm) [37]

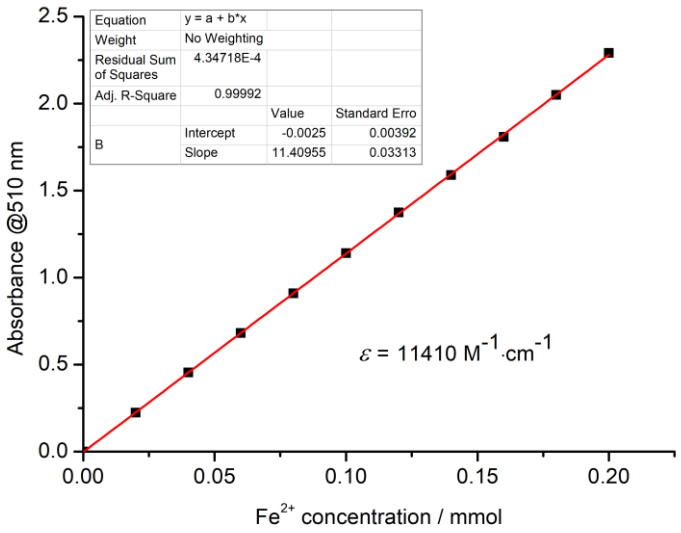

Figure 65. Calibration chart plotting the concentration of Fe^{2+} ions against the absorbance at 510 nm.[38] This graph was utilized to determine the extinction coefficient of the ferrioxalate-phenanthroline complex, also known as ferroin, at 510 nm. The calibration solutions were prepared by diluting a commercially available 0.1 mol/L $FeSO_4$ solution (purchased from Hayashi Pure Chemical, Lot No T211109001) in a sodium acetate buffer containing phenanthroline (0.1 wt%, 300 μL).

6. Synthesis

Synthesis of 1

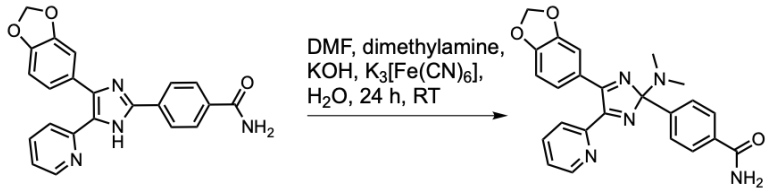

Scheme 2. Synthetic scheme for **1**.

SB431542 (40 mg, 0.104 mmol) and dimethylamine (1.04 mmol, which was procured as a solution in *N, N*-dimethylformamide (DMF)) were mixed. To this solution, 10.6 mL aqueous solution containing KOH (0.75 g, 13.4 mmol) and $K_3[Fe(CN)_6]$ (1.49 g, 4.7 mmol) was added. The reaction mixture was stirred vigorously under nitrogen atmosphere at room temperature for 24 h. The progress of the reaction was monitored using reverse phase thin-layer chromatography (TLC) with an eluent system of water:acetonitrile (1:1). Upon completion of the reaction, 10 mL of water was added to the reaction mixture. The resulting reaction mixture was extracted with ethyl acetate (20 mL × 3). The organic extracts were combined, dried over anhydrous $MgSO_4$, evaporated, and subsequently subjected to purification using gradient high-performance liquid chromatography (HPLC) employing a solvent gradient of 30 - 70% acetonitrile in water over a period of 4 hours at a flow rate of 10 mL/min. This purification afforded **1** as a pale-yellow powder (6.1 mg, yield = 14%).

^{1}H NMR (400 MHz, D_2O:Acetonitrile-d_3 (1:1)): δ ppm 8.50 - 8.46 (m, 2H), 8.42 (m, 1H), 8.20 - 8.17 (m, 1H), 8.06 - 8.02 (m, 2H), 7.92 (d, J = 1.7 Hz, 1H), 7.77 (td, J = 8.0, 1.9 Hz, 2H), 7.61 (dt, J = 8.0, 1.1 Hz, 1H), 7.3 - 7.28 (m, 2H), 6.94 (d, J = 8.3 Hz, 1H), 6.05 (dd, J = 5.2, 0.9 Hz, 2H), 2.40 (s, 6H).

^{13}C NMR (400 MHz, D_2O:Acetonitrile-d_3 (1:1)): δ ppm 198.66, 193.19, 175.98, 173.58, 170.66, 154.64, 152.21, 149.47, 147.97, 138.24, 136.29, 134.15, 129.47, 128.21, 126.67, 124.13, 124.02, 122.47, 108.51, 106.69, 102.43, 40.01.

High resolution mass spectra (ESI) of **1** - m/z $[M+H]^+$ calculated for $C_{24}H_{21}N_5O_3$: 428.17226, found: 428.17092; m/z $[M+Na]^+$ calculated: 450.15421, found: 450.15276.

Synthesis of 2

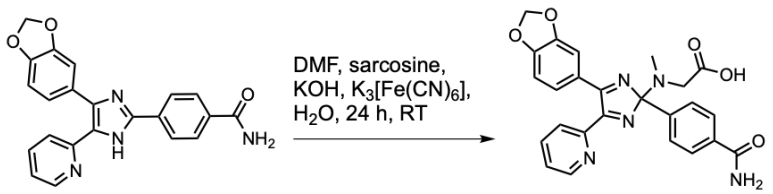

Scheme 3. Synthetic scheme for **2**.

SB431542 (100 mg, 0.26 mmol) was dissolved in 4 mL of *N, N*-dimethylformamide (DMF). To this solution, 27 mL of aqueous solution containing KOH (1.89 g, 33.7 mmol), $K_3[Fe(CN)_6]$ (3.78 g, 11.34 mmol) and sarcosine (236.7 mg, 2.66 mmol) was added. The reaction mixture was vigorously stirred under nitrogen atmosphere at room temperature for 24 h. Reverse phase TLC analysis (using a water:acetonitrile eluent system, 1:1) was employed to monitor the reaction progress. Upon completion, 20 mL of water was added to the reaction mixture. The resultant reaction mixture was extracted with ethyl acetate (40 mL × 3). The combined organic extracts were dried over anhydrous $MgSO_4$, evaporated, followed by purification using gradient high-performance liquid chromatography (HPLC) employing a solvent gradient of 30 - 70% acetonitrile in water over a 4-hour period at a flow rate of 10 mL/min. This purification process afforded **2** as a pale-yellow powder (6.0 mg, yield = 4.9%).

^{1}H NMR (400 MHz, D_2O:Acetonitrile-d_3 (1:1)) δ ppm 8.57 (d, J = 4.8 Hz, 1H), 8.04 – 7.99 (m, 1H), 7.91 – 7.75 (m, 5H), 7.63 – 7.58 (m, 1H), 7.06 – 6.98 (m, 2H), 6.85 (dd, J = 8.2, 1.2 Hz, 1H), 6.03 (d, J = 1.5 Hz, 2H), 2.31 (d, J = 1.2 Hz, 5H).

^{13}C NMR (400 MHz, D_2O:Acetonitrile-d_3 (1:1)) δ ppm 168.25, 164.75, 164.48, 152.12, 149.98, 148.94, 147.63, 142.65, 137.25, 134.17, 128.66, 128.03, 127.18, 125.91, 125.11, 124.45, 124.44, 109.15, 107.75, 102.04, 38.64.

High resolution mass spectra (ESI) of **2** - m/z $[M+H]^+$ calculated for $C_{25}H_{21}N_5O_5$: 472.16209, found: 428.17077 indicating the elimination of a molecule of CO_2 $[M+H-CO2]^+$; m/z $[M+Na]^+$ calculated: 494.14404 found: 450.15237 indicating the elimination of a molecule of CO_2 $[M+Na-CO_2]^+$.

Synthesis of 3

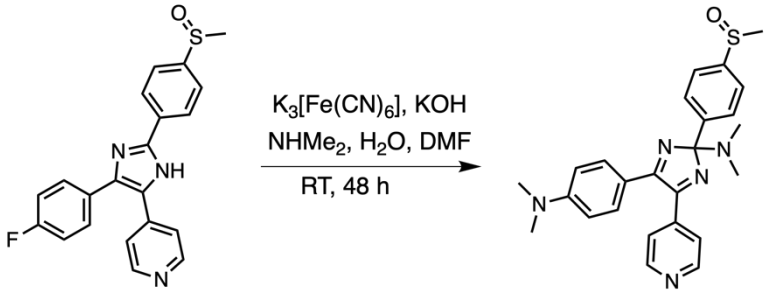

Scheme 5. Synthetic scheme for **3**.

Adezmapimod (75 mg, 0.2 mmol) and 4.5 mL of dimethylamine (0.68 mmol, which was procured as a solution in *N, N*-dimethylformamide (DMF)) were mixed. To this solution, 19.9 mL of aqueous solution containing KOH (0.14 g, 2.52 mmol) and $K_3[Fe(CN)_6]$ (2.81 g, 8.52 mmol) was added and stirred for 48 h under nitrogen atmosphere. The reaction was monitored using normal phase TLC with ethyl acetate and triethylamine (97:3) eluent system. Upon completion of the reaction 15 mL of water was added to the reaction mixture and extracted with ethyl acetate (30 mL × 3). The organic layers were combined and dried over anhydrous $MgSO_4$ and evaporated. The crude compound was later purified by preparative HPLC employing a solvent gradient of 30 - 60% acetonitrile in water over a 3 h period at a flow rate of 5 mL/min. This purification process afforded **3** as a pale-yellow powder (3 mg, yield = 3.4%).

^{1}H NMR (600 MHz, D_2O:Acetonitrile-d_3 (1:1)): δ ppm 8.55 (d, J = 6.6 Hz, 2H), 8.43 (d, J = 5.4 Hz, 2H), 8.26 (d, J = 8.4 Hz, 2H), 7.91 (d, J = 7.8 Hz, 2H), 7.44 (d, J = 5.4 Hz, 2H), 6.73 (d, J = 7.2 Hz, 2H), 3.03 (s, 6H), 2.89 (s, 3H), 2.40 (s, 6H).

^{13}C NMR (600 MHz, CD_3OD): δ ppm 194.87, 175.80, 155.58, 150.81, 150.57, 150.11, 149.54, 135.75, 133.04, 132.83, 131.62, 131.47, 125.37, 123.71, 118.57, 112.20, 105.94, 40.96, 40.31, 40.08, 30.92.

High resolution mass spectra (ESI) of **3** - m/z $[M+Na]^+$ calculated for $C_{25}H_{27}N_5OS$: 468.18340, found: 468.18191.

Synthesis of 4

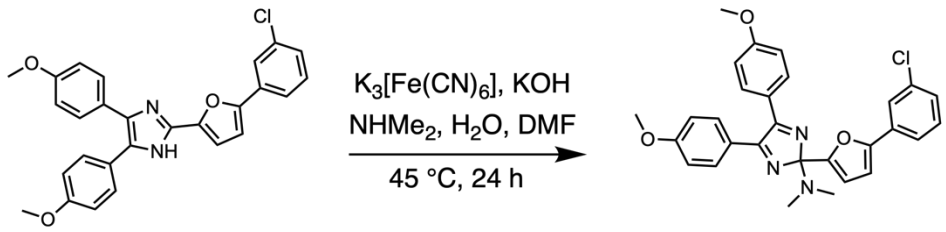

Scheme 6. Synthetic scheme for **4**.

Neurodazine (28.6 mg, 0.063 mmol) and dimethylamine (0.63 mmol, which was procured as a solution in *N, N*-dimethylformamide (DMF)) were mixed. To this solution, 1 mL aqueous solution containing KOH (0.07 g, 0.13 mmol) and $K_3[Fe(CN)_6]$ (0.15 g, 0.45 mmol) was added. The reaction mixture was stirred vigorously at 45 °C for 24 h. The progress of the reaction was monitored using reverse phase thin-layer chromatography (TLC) with an eluent system of water:acetonitrile (2:8). Upon completion of the reaction, 10 mL of water was added to the reaction mixture. The resulting reaction mixture was extracted with ethyl acetate (20 mL × 3). The organic extracts were combined, dried over anhydrous $MgSO_4$, evaporated, and subsequently subjected to purification using gradient high-performance liquid chromatography (HPLC) employing a solvent gradient of 50 - 80% acetonitrile in water over a period of 4 hours at a flow rate of 10 mL/min. This purification afforded **4** as a pale-yellow powder (2 mg, yield = 7%).

^{1}H NMR (600 MHz, Acetonitrile-d_3) δ 7.69 (s, 1H), 7.63 (dd, J = 7.9, 1.5 Hz, 1H), 7.53 – 7.51 (m, 4H), 7.43 – 7.39 (m, 1H), 7.32 – 7.29 (m, 1H), 6.97 – 6.94 (m, 4H), 6.80 (dd, J = 3.5, 1.1 Hz, 1H), 6.52 (dd, J = 3.5, 1.1 Hz, 1H), 3.83 (d, J = 1.2 Hz, 6H), 2.39 (d, J = 1.1 Hz, 6H).

^{13}C NMR (600 MHz, Acetonitrile-d_3) δ 167.26, 162.71, 153.31, 152.57, 135.34, 133.42, 131.76, 125.49, 124.34, 122.92, 114.88, 114.81, 114.59, 114.52, 56.15, 39.78.

High resolution mass spectra (ESI) of **4** - m/z $[M+H]^+$ calculated for $C_{29}H_{26}ClN_3O_3$:

500.17409, found: 500.17337.

Synthesis of 5

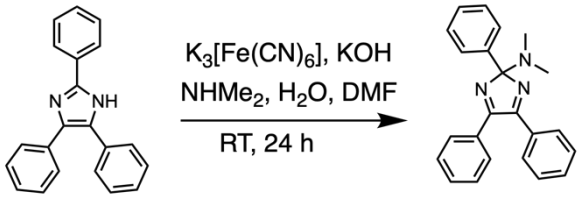

Scheme 7. Synthetic scheme for **5**.

Lophine (1 g, 3.37 mmol) and dimethylamine (33.7 mmol, which was procured as a solution in *N, N*-dimethylformamide (DMF)) were mixed. To this solution, 337.4 mL aqueous solution containing KOH (23.59 g, 421.2 mmol) and $K_3[Fe(CN)_6]$ (47.18 g, 143.3 mmol) was added. The reaction mixture was stirred vigorously under nitrogen atmosphere at room temperature for 24 h. The progress of the reaction was monitored using thin-layer chromatography (TLC) with an eluent system of 2% methanol in dichloromethane. Upon completion of the reaction, 200 mL of water was added to the reaction mixture. The resulting reaction mixture was extracted with ethyl acetate (200 mL × 3). The organic extracts were combined, dried over anhydrous $MgSO_4$, evaporated, and subsequently subjected to purification using normal phase silica gel column chromatography using 1% methanol in dichloromethane as eluent. This purification afforded a pale-yellow powder (0.276 g, yield = 24.2%).

^{1}H NMR (400 MHz, Acetonitrile-d_3) δ 8.47 – 8.44 (m, 2H), 8.42 – 8.39 (m, 2H), 7.66 – 7.60 (m, 3H), 7.54 – 7.50 (m, 1H), 7.48 (m, 1H), 7.47 – 7.43 (m, 3H), 7.27 – 7.19 (m, 3H), 2.42 (s, 6H).

^{13}C NMR (600 MHz, Methanol-d_4) δ 196.55, 174.89, 136.94, 133.88, 133.27, 132.39, 132.07, 130.63, 130.55, 130.47, 130.42, 130.33, 129.91, 129.64, 129.57, 129.49, 128.02, 127.94, 107.54, 40.80, 40.74.

High resolution mass spectra (ESI) of **5** - m/z $[M+H]^+$ calculated for $C_{23}H_{21}N_3$: 340.18137, found: 340.18022.

7. Acknowledgement

This dissertation would not be done without the guidance and the help of several individuals who contributed and extended their assistance in this study. It is a pleasure to convey my appreciation to them all in my humble acknowledgment.

This dissertation is completed because of the support and ideas of my supervisor, Professor Nobuyuki Tamaoki. Without his supervision, advice and suggestions in this research, I could not have finished this task. I would like to express great pleasure to acknowledge with deep sense of gratitude and sincere appreciation to him for giving me extraordinary experiences through the research. Above all, he taught me not only theoretical and practical knowledge, but also how to become a responsible researcher in the future.

I deem it a pleasure and express my deep sense of gratitude and humble regards to Dr. Amrutha A S, whose able guidance, keen interest, aesthetic suggestions and constant supervision helped me throughout the work. Her constant support and inspiring guidance were very helpful for me not only in this work but also for my academic life.

I thank to Dr. P. K. Hashim for whom I can always ask if I have any problem. He is wise and have profound knowledge. He can not only anwser the questions I have, also make me get to know how to solve this kind of problem.

I am grateful to Dr. Sumire Ishida-Ishihara, who taught me about conducting cell experiments starting from scratch.

I want to thank Professor Masumi Tsuda for teaching me Immunoblotting analysis and giving me a chance to learn more about protein experiments.

I would like to thanks Professor Hiroshi Hirata. He taught and helped me about the Electron spin resonance experiment.

In my lab, I had the company of a friendly and cheerful group. Everyone of them helped me and provide me a good lab environment. I would like to thank all the members, Dr. Runze Lin, Dr. Saugta Sahu, Mrs. Madappuram Cheruthu Nusaiba, Ms Shifa Ahmad, Ms Chuhan Xu for their kind experimental supports and daily help.

I would like to thank Hokkaido University for giving me the opportunity to study in Japan and learn the culture of Japan. I also want to express my gratitude to Hokkaido University DX Doctoral fellowship for supporting my research and living expenses.

My family needs special mention for their support. My parents always support me without any complaint. They encouraged me all my life.

I thank my cat GUMI for keeping me happy and energetic everyday.

JiaJun Qi

8. Abbreviations

DMF - *N*, *N*-dimethylformamide

DMSO - dimethylsulfoxide

HABI – hexaarylbiimidazole

HPLC – high-performance liquid chromatography

PDT - photodynamic therapy

TGF-β1 - Transforming growth factor β1

TGF-β R1 - Transforming growth factor β receptor 1

9. References

1. Liu, G.; Chen, T.; Zhang, X.; Ma, X.; Shi, H. Small molecule inhibitors targeting the cancers. *MedComm* **2022**, *3*, e181.
2. Lavanya, V.; Adil, M.; Ahmed, N.; Rishi, A. K.; Jamal, S. Small molecule inhibitors as emerging cancer therapeutics. *Integr. Cancer Sci. Ther.* **2014**, *1*, 39-46.
3. Zhong, L.; Li, Y.; Xiong, L.; Wang, W.; Wu, M.; Yuan, T.; Yang, W.; Tian, C.; Miao, Z.; Wang, T.; Yang, S. Small molecules in targeted cancer therapy: advances, challenges, and future perspectives. *Signal Transduct. Target. Ther.* **2021**, *6*, 201.
4. Allen, T. M.; Cullis, P. R. Drug delivery systems: entering the mainstream. *Science* **2004**, *303*, 1818-1822.
5. Mura, S.; Nicolas, J.; Couvreur, P. Stimuli-responsive nanocarriers for drug delivery. *ACS Nano* **2013**, *12*, 991-1003.
6. Schmaljohann, D. Thermo- and pH-responsive polymers in drug delivery. *Adv. Drug Deliv. Rev.* **2006**, *58*, 1655-1670.
7. Rwei, A. Y.; Wang, W.; Kohane, D. S. Photoresponsive nanoparticles for drug delivery. *Nano Today* **2015**, *10*, 451–467.
8. Deisseroth, K. Optogenetics. *Nat. Methods* **2011**, *8*, 26-29.

9. Correia, J. H.; Rodrigues, J. A.; Pimenta, S.; Dong, T.; Yang, Z. Photodynamic therapy review: principles, photosensitizers, applications, and future Directions. *Pharmaceutics* **2021**, *13*, 1332.
10. (a)Velema, W. A.; Szymanski, W.; Feringa, B. L. Photopharmacology: beyond proof of principle. *J. Am. Chem. Soc.* **2014**, *136*, 2178–2191. (b) Lerch, M. M.; Hansen, M. J.; van Dam, G. M.; Szymanski, W.; Feringa, B. L. Emerging targets in photopharmacology. *Angew. Chem. Int. Ed.* **2016**, *55*, 10978–10999. (c) Hüll, K.; Morstein, J.; Trauner, D. In vivo photopharmacology. *Chem. Rev.* **2018**, *118*, 10710−10747. (d) Fuchter, M. J. On the Promise of Photopharmacology Using Photoswitches: A Medicinal Chemist's Perspective. *J. Med. Chem.* **2020**, *63*, 11436–11447.
11. (a) Liu, J.; Kang, W.; Wang, W. Photocleavage-based photoresponsive drug delivery. *Photochem. Photobiol*. **2022**, *98*, 288-302. (b) Klán, P.; Šolomek, T.; Bochet, C. G.; Blanc, A.; Givens, R.; Rubina, M.; Popik, V.; Kostikov, A.; Wirz, J. Photoremovable protecting groups in chemistry and biology: reaction mechanisms and efficacy. *Chem. Rev*. **2013**, *113*, 119–191. (c) Ma, X.; Johnson, D. A.; He, X. J.; Layden, A. E.; McClain, S. P.; Yung, J. C.; Rizzo, A.; Bonaventura, J.; Banghart, M. R. In vivo photopharmacology with a caged mu opioid receptor agonist drives rapid changes in behavior. *Nat. Methods* **2023**, *20*, 682-685. (d) Sekhar, A. R.; Chitose, Y.; Janoš, J.; Dangoor, S. I.; Ramundo, A.; Satchi-Fainaro, R.; Slavíček, P.; Klán, P.; Weinstain, R. Porphyrin as a versatile visible-light-activatable organic/metal hybrid photoremovable protecting group. *Nat. Commun*. **2022**, *13*, 3614.
12. (a) Kobauri, P.; Dekker, F. J.; Szymanski, W.; Feringa, B. L. Rational design in photopharmacology with molecular photoswitches. *Angew. Chem. Int. Ed.* **2023**, *135*, e202300681. (b) Zhang, Z.; Le, G. N. T.; Ge, Y.; Tang, X.; Chen, X.; Ejim, L.; Bordeleau, E.; Wright, G. D.; Burns, D. C.; Tran, S.; Axerio-Cilies, P; Wang, Y. T.; Dong, M.; Woolley, G. A. Isomerization of bioactive acylhydrazones triggered by light or thiols. *Nat. Chem.*, **2023**, *15*, 1285-1295. (c) Prischich, D.; Camarero, N.; Encinar del Dedo, J.; Giralt, E.; Geli, M. I.; Gorostiza, P. Light-dependent inhibition of clathrin-

mediated endocytosis in yeast unveils conserved functions of the AP2 complex. *iScience* **2023**, *26*, 107899. (d) Josa-Culleré, L.; Llebaria, A. Visible-light-controlled histone deacetylase inhibitors for targeted cancer therapy. *J. Med. Chem*. **2023**, *66*, 1909–1927. (e) Baumgartner, B.; Glembockyte, V.; Mayer, R.; Gonzalez-Hernandez, A.; Kindler, R.; Valavalkar, A.; Wiegand, A.; Müller-Deku, A.; Grubert, L.; Steiner, F.; Gross, C.; Reynders, M.; Grenier, V.; Broichhagen, J.; Hecht, S.; Tinnefeld, P.; Ofial, A.; Dietzek-Ivanšic, B.; Levitz, J.; Thorn-Seshold, O. Azobenzenes can achieve near-infrared photocontrol in biological systems, with quantitative Z → E photoisomerization, via singlet manifold photoredox. *ChemRxiv* [Working Paper], Version 1; September 14, **2023**. (f) Impastato, A. C.; Shemet, A.; Vepřek, N. A.; Saper, G.; Hess, H.; Rao, L.; Gennerich, A.; Trauner, D. Optical control of mitosis with a photoswitchable Eg5 inhibitor. *Angew. Chem. Int. Ed.* **2022**, *61*, e2021158. (g) Mafy, N. N.; Matsuo, K.; Hiruma, S.; Uehara, R.; Tamaoki, N. Photoswitchable CENP-E inhibitor enabling the dynamic control of chromosome movement and mitotic progression. *J. Am. Chem. Soc.* **2020**, *142*, 1763–1767.

13. Le Bescont, J.; Mouawad, L.; Boddaert, T.; Bombard, S.; Piguel, S. Photoactivatable small-molecule inhibitors for light-controlled TAM kinase activity. *ChemPhotoChem* **2021**, *5*, 989–994.
14. Horbert, R.; Pinchuk, B.; Davies, P.; Alessi, D.; Peifer, C. Photoactivatable prodrugs of antimelanoma agent vemurafenib. *ACS Chem. Biol*. **2015**, *10*, 2099−2107.
15. Wang, H.; Chen, M.; Sang, X.; You, X.; Wang, Y.; Paterson, I. C.; Hong, W.; Yang, X. Development of small molecule inhibitors targeting TGF-β ligand and receptor: structures, mechanism, preclinical studies, and clinical usage. *Eur. J. Med. Chem*. **2020**, *191*, 112154-112165.
16. Ali, I.; Lone, M. N.; Aboul-Enein, H. Y. Imidazoles as potential anticancer agents. *Med. Chem. Commun.* **2017**, *8*, 1742-1773.
17. Halder, S. K.; Beauchamp, R. D.; Datta, P. K. A specific inhibitor of TGF-β receptor kinase, SB-431542, as a potent antitumor agent for human cancers. *Neoplasia* **2005**, *7*, 509–521.

18. Inman, G. J.; Reith, A. D.; Laping, N. J.; Hill, C. S. SB-431542 Is a Potent and specific inhibitor of transforming growth factor-β superfamily type I activin receptor-like kinase (ALK) receptors ALK4, ALK5, and ALK7. *Mol. Pharmacol*. **2002**, *62*, 65-74.
19. Chaudhury, A.; Howe, P. H. The Tale of transforming growth factor-beta (TGFβ) signalling: a soigné enigma. *IUBMB Life* **2009**, *61*, 929–939.
20. Tzavlaki, K.; Moustakas, A. TGF-β signaling. *Biomolecules* **2020**, *10*, 487.
21. Kubiczkova, L.; Sedlarikova, L.; Hajek, R.; Sevcikova, S. TGF-β – an excellent servant but a bad master. *J. Transl. Med*. **2012**, *10*, 183.
22. Josa-Culler, L.; Llebaria, A. In the search for photocages cleavable with visible light: an overview of recent advances and chemical strategies. *ChemPhotoChem* **2021**, *5*, 296–314.
23. (a) Albers, R. E.; Selesneimi, K.; Natale, D. R. C.; Brown, T. L. TGF-β induces Smad2 Phosphorylation, ARE Induction, and Trophoblast Differentiation. *Int. J. Stem Cells* **2018**, *11*, 111-120. (b) Derynck, R.; Zhang, Y. E. Smad-dependent and Smad-independent pathways in TGF- β family signalling. *Nature* **2003**, *425*, 577-584.
24. Ramirez, H.; Patel, S. B.; Pastar, I. The role of TGF signaling in wound epithelialization. *Adv. Wound Care (New Rochelle)*. **2014** *3*, 482-491.
25. Tie, Y.; Tang, F.; Peng, D.; Zhang, Y.; Shi, H. TGF-beta signal transduction: biology, function, and therapy for diseases. *Mol. Biomed*. **2022**, *3*, 45-73.
26. Jonkman, J. E. N.; Cathcart, J. A.; Xu, F.; Bartolini, M. E.; Amon, J. E.; Stevens, K. M.; Colarusso, P. An introduction to the wound healing assay using live-cell microscopy. *Cell Adhes. Migr*. **2014**, *8*, 440–451.
27. Ogunjimi, A. A.; Zeqiraj, E.; Ceccarelli, D. F.; Sicheri, F.; Wrana, J. L.; David, L. Structural basis for specificity of TGFβ family receptor small molecule inhibitors. *Cell. Signal*. **2012**, *24*, 476–483.
28. Paw, M.; Wnuk, D.; Nit, K.; Bobis-Wozowicz, S.; Szychowski, R.; Ślusarczyk, A.; Madeja, Z.; Michalik, M. SB203580—A Potent p38 MAPK inhibitor reduces the profibrotic bronchial fibroblasts transition associated with asthma. *Int. J. Mol. Sci*. **2021**, *22*, 12790-12806.

29. Kim, G.H.; Halder, D.; Park, J.; Namkung, W.; Shin, I. Imidazole-Based Small Molecules that Promote Neurogenesis in Pluripotent Cells. *Angew. Chem. Int. Ed.* **2014**, *53*, 9271–9274.
30. (a) Lombardino, J. G.; Wiseman, E. H. Preparation and anti-inflammatory activity of some nonacidic trisubstituted imidazoles. *J. Med. Chem.* **1974**, *17*, 1182-1188. (b) Astles, P. C.; Ashton, M. J.; Bridge, A. W.; Harris, N. V.; Hart, T. W.; Parrott, D. P.; Porter, B.; Riddell, D.; Smith, C.; Williams, R. J. Acyl-CoA:Cholesterol O-Acyltransferase (ACAT) inhibitors. 2.2-(1,3-Dioxan-2-yl)-4,5-diphenyl-1H-imidazoles as potent inhibitors of ACAT. *J. Med. Chem.* **1996**, *39*, 1423-1432. (c) Doble, M.; Puratchikody, A. Antinociceptive and anti-inflammatory activities and QSAR studies on 2-substituted-4,5-diphenyl-1H-imidazoles. *Bioorg. Med. Chem.* **2007**, *15*, 1083-1090. (d) Gurjar, A. S.; Darekar, M. N.; Yeong, K. Y.; Ooi, L. In silico studies, synthesis, and pharmacological evaluation to explore multi-targeted approach for imidazole analogues as potential cholinesterase inhibitors with neuroprotective role for Alzheimer's disease. *Bioorg. Med. Chem.* **2018**, *26*, 1511-1522.
31. (a) Hayashi, T.; Maeda, K. Preparation of a new phototropic substance. *Bull. Chem. Soc. Jpn.* **1960**, *33*, 565-566. (b) White, D. M.; Sonnenberg, J. Oxidation of Triarylimidazoles. Structures of the Photochromic and Piezochromic Dimers of Triarylimidazyl Radicals. *J. Am. Chem. Soc.* **1966**, *88*, 3825-3829. (c) Tanino, H.; Kondo,T.; Okada, K.; Goto, T. Structures of Three Isomeric Dimers of 2,4,5-Triphenylimidazolyl. *Bull. Chem. Soc. Jpn.* **1972**, *45*, 1474-1480. (d) Kishimoto, Y.; Abe, J. A fast photochromic molecule that colors only under UV light. *J. Am. Chem. Soc.* **2009**, *131*, 4227–4229.
32. Sakaino, Y.; Kakisawa, H.; Kusumi, T. Synthesis of new photochromic compounds from the dimer of arylphenanthroimidazoles. *J. Heterocycl. Chem.* **1975**, *12*, 953–956.
33. Madgzinski, L. J.; Pillay, K. S.; Richard, H.; Chow, Y. L. Decomposition of tetramethyl-2-tetrazene under acidic conditions. *Can. J. Chem.*, **1978**, *56*, 1657-1667.
34. (a) Shin, G.; Gomez, A. M.; Al-Hasani, R.; Jeong, Y. R.; Kim, J.; Xie, Z.; Banks, A.; Lee, S. M.; Han, S. Y.; Yoo, C. J.; Lee, J.; Lee, S. H.; Kurniawan, J.; Tureb, J.; Guo, Z.;

Yoon, J.; Park, S-I.; Bang, S.Y.; Nam, Y.; Walicki, M. C.; Samineni, V.K.; Mickle, A.D.; Lee, K.; Heo, S.Y.; McCall, J.G.; Pan, T.; Wang, L.; Feng, X.; Kim, T-I; Kim, J.K.; Li, Y.; Huang, Y.; Gereau, R. W. IV; Ha, J. S.; Bruchas, M. R.; Rogers, J. A. Flexible Near-Field Wireless Optoelectronics as Subdermal Implants for Broad Applications in Optogenetics. *Neuron*, **2017**, *93*, 509-521. (b) Karatum, O.; Gwak, M-J.; Hyun, J.; Onal, A.; Koirala, G. R.; Kim, T-i.; Nizamoglu, S. Optical neuromodulation at all scales: from nanomaterials to wireless optoelectronics and integrated systems. *Chem. Soc. Rev*., **2023**, *52*, 3326-3352.

35. Sun, B.; Teo, J. Y.; Wu, J.; Zhang, Y. Light conversion nanomaterials for wireless phototherapy. *Acc. Chem. Res*. **2023**, *56*, 1143-1155.

36. Trott, O.; Oslon, A. J. AutoDock Vina: Improving the speed and accuracy of docking with a new scoring function, efficient optimization, and multithreading. *J. Comput. Chem.* **2009**, *31*, 455-461.

37. Hatchard, C. G.; Parker, C. A. A new sensitive chemical actinometer-II. Potassium ferrioxalate as a standard chemical actinometer. *Proc. R. Soc. Lond. A* **1956**, *235*, 518–536.

38. Lin, R.; Hashim, P. K.; Sahu, S.; Amrutha, A. S.; Cheruthu, N. M.; Thazhathethil, S.; Takahashi, K.; Nakamura, T.; Kikukawa, T.; Tamaoki, N. Phenylazothiazoles as Visible-Light Photoswitches. *J. Am. Chem. Soc*. **2023**, *145*, 9072-9080.